Yearly Progress Report (May 2020):
Plasma Surface Interactions: Predicting the Performance and Impact of Dynamic PFC Surfaces

Lead PI: Brian Wirth, UTK-ORNL Governor's Chair Professor of Computational Nuclear Engineering

Institution – Agreement/FWP #	*Principal Investigator*	*Senior Personnel*
ORNL - ERAT953	Brian Wirth	David Bernholdt, John Canik, Philip Fackler, David Green, Cory Hauck, James Kress, Jeremy Lore, David Pugmire, Phil Roth, Pablo Seleson, Tim Younkin
ANL –	Barry Smith	
LLNL - SCW1617 / SCW1620	Ilon Joseph	Mikhail Dorf, Milo Dorr, Debojyoti Ghosh, Maxim Umansky
LANL -	Enrique Martinez	Zachary Bergstrom, Sham Bhat, Eduard Kober, Nithin Matthew, Danny Perez
PNNL – FWPs 70444/70230	Wahyu Setyawan	Giridhar Nandipati, Ken Roche
SNL – FWPs 18-020352/18-020349	Habib Najm	Tiernan Casey, Mary Alice Cusentino, Khachik Sargsyan, Aidan Thompson, Mitch Wood
GA – DE-SC0018423	Phil Snyder	Rui Ding, Jerome Guterl, Orso Meneghini
University of California, San Diego (UCSD) – DE-SC0018302	Sergei Krasheninnikov	Russ Doerner, Roman Smirnov
University of Illinois, Urbana-Champaign (UIUC) – DE-SC0018141	Davide Curreli	Jon Drobny, Fazlul Md Huq, Mohammad Mustafa
University of Massachusetts, Amherst – DE-SC0018421	Dimitrios Maroudas	Chao-Shou Chen, Asanka Weerasinghe
University of Missouri	Karl Hammond	Brandon Laufer
University of Tennessee, Knoxville	Brian Wirth	Sophie Blondel, Dwaipayan Dasgupta, Alyssa Hayes, Ane Lasa, David Martin, Li Yang
Rennselaer Polytechnic Institute (RPI)[•]	Mark Shephard	Max Bloomfield, Dhyanjyoti Nath, Gopan Perumpilly, Onkar Sahni, Cameron Smith
University of California, Los Angeles (UCLA)[·]	Jaime Marian	Qianran Yu

Executive Summary

This document describes the integrated project progress during the third year of the project, focusing on the time period May 2019 – April 2020. Overall, the PSI SciDAC project had a very productive and impactful year (May 2019 – April 2020), with highlights including:

[•] RPI receives separate SciDAC-4 funding, but is integrated into project and the RPI contributions to our project are included in this report.

[·] UCLA was not funded as part of SciDAC-4 project, but through FES programmatic funds with intention of coordinating with the PSI SciDAC, and thus their contributions are included in this report.

- Publication of 28 peer-reviewed, archival journal publications in 2019 and 2020, as listed in Appendix 1; one of which was an Editor's pick (Smirnov et al., *Physics of Plasmas* **27** (2020) 032503), and several of which describe experimental validation of modeling predictions;
- Interactions with both DIII-D (General Atomics) and WEST (CEA-Cadarache, France) tokamaks for experimental validation of PSI predictions;
- Strong engagement with the ITER Divertor and Plasma-Wall Interactions Section associated with assessing role of neon radiative divertor injection (seeding) on minimizing the peak divertor heat flux;
- Multiple oral presentations and strong project presence at the 2019 Plasma Facing Components Conference in Eindhoven, Netherlands in May;
- Strong engagement of CS/AM researchers into code development of GITR and hPIC to utilize unstructured meshes, code development of Xolotl for efficient utilization of GPUs, and of UQ and sensitivity analysis within several research tasks; and
- Participation in the 17th International Workshop on Plasma Edge Theory in Fusion Devices (August 2019, La Jolla, CA) and 61st Annual Meeting of the APS Division of Plasma Physics (October 2019, Florida).

The remainder of this document presents a brief review of the project objectives, before providing a concise summary of the research activities as organized by research task (Note that in the interest of brevity, this summary is not comprehensive, but rather conveys highlights of research activities to provide an indication of the breadth of the project activities), and then concludes with the next steps planned for each task and a review of the status of our proposed milestones for project years 4 and 5.

Introduction and Background

The objective of this project is to develop, and integrate, high-performance simulation tools capable of predicting plasma facing component (PFC) operating lifetime and the impact of the evolving surface morphology of tungsten-based PFCs on plasma contamination, including the dynamic recycling of fuel species and tritium retention, in future magnetic fusion devices. Establishing a fundamental physical understanding and developing predictive capabilities of plasma-surface interactions (PSI) requires simultaneously addressing complex and diverse physics occurring over a wide range of length (Angstroms to meters) and time (femtoseconds to years) scales, as well as integrating extensive physical processes across the plasma – surface interface. This requires development of not only detailed physics models and computational strategies at each scale, but also algorithms and methods to couple them effectively in a way that can be robustly validated. Deploying these tools requires the continued development and coupling of leadership-scale computational codes to describe the boundary plasma and the evolving PFC surface, as well as a host of simulations that bridge disparate scales to address complex physical and computational issues at the plasma – surface interface in multi-component materials systems for magnetic fusion energy development beyond ITER.

This project will enable discovery of the key physical phenomena controlling critical PFC performance issues, and the quantitative prediction of their impact on PFC performance during both steady-state and transient plasma conditions. Such phenomena include: (i) surface evolution in regions of either net erosion or net deposition; (ii) the impact of the evolving surface composition and roughness on the retention and recycling of hydrogenic fuel isotopes; (iii) the impact of dilute impurities on surface morphological evolution and plasma contamination; and (iv) the effects of high-energy neutron damage on surface properties that could influence helium/hydrogenic species retention and recycling. The research activities within this proposed project will focus on three broadly defined research thrusts:

- Bridging the scales between atomistic/microstructural modeling and the continuum-based PFC simulations through the adaptation of multiscale modeling techniques. Specifically, *ab initio*/atomistic/microstructural studies will be used to develop the requisite knowledge to 'coarse

grain' disparate, heterogeneous material structures and 'scale bridge' across diverse spatial/temporal scales to provide detailed input to, and calibrate, the Xolotl PFC simulator;

- Integrating boundary plasma and surface evolution models, specifically investigating effects of the plasma sheath and evolving surfaces, in order to predict PFC performance under both steady-state plasma operation and in the presence of transient events. This includes the development of a new code to model the fate of eroded impurities, including their migration and re-deposition, specifically designed to take advantage of leadership-class computing facilities; and
- Studying the dynamic response of the surface to transient plasma events and exploring synergistic phenomena between the near-surface plasma and wall response, with emphasis on dynamic recycling processes that couple the divertor plasma to the material surface layer. The coupled models will explore the impact of wall response on boundary turbulence and divertor detachment dynamics.

The outcome of this project will be a suite of coupled plasma and materials modeling tools, and a leadership class PFC simulator to predict PFC evolution and feedback to the boundary plasma both during steady-state plasma operation and transient events. Towards this end, we plan to have strong coordination of our efforts with the other successful fusion SciDAC projects proposals in the Boundary Physics and Whole Device Modeling topical areas. Success in the proposed research tasks will enable the prediction of both plasma fueling and the sources of impurity contamination that impact core plasma performance, and will lay the foundation for understanding, designing and developing the materials required to meet the performance objectives of future fusion reactors.

The project has a web presence at: https://collab.cels.anl.gov/display/PSIscidac2/ leveraging R&D infrastructure available in the ANL Mathematics and Computer Sciences Division. This wiki site has both public-facing and project-private spaces. Currently, the public space provides basic information about project goals, participants, sponsors, key collaborators, and a catalog of project presentations and publications. The private space includes records of project and working group meetings and other information. Additionally, we use a Subversion repository, also hosted at ANL, as a repository for internal and under-development documents, and the project mailing list hosted at ORNL.

This document describes the integrated project progress during the third year time period from May 2019 – April 2020, and includes discussion on the status of specific activities, and then concludes with the next steps planned for each task and a review of the status of our proposed milestones for project years 4 and 5.

STATUS AND PROGRESS ON PROJECT RESEARCH ACTIVITIES

Computer Science/Applied Math

Computer science and applied math (CS/AM) are strongly driven by the science goals of the project and are well integrated through the three major Tasks described below. In this section, we call out and describe certain of these activities in greater detail in order to illustrate the engagement and interactions within the project. We would also like to note our engagement with researchers at Rensselaer Polytechnic Institute (RPI) as part of Task 2, where the current focus is on infrastructure development in support of parallel, unstructured meshing in two PSI codes, GITR and hPIC. A brief summary of their work is included here and is more fully reported in their own progress report, which encompasses their work on multiple SciDAC projects.

Summary of Accomplishments (May 2019-April 2020):

- Performance analysis of SNAP potentials in LAMMPS has yielded insights that will allow performance optimizations in the future.
- Excellent progress is being made on porting Xolotl to use GPUs. Management and evaluation of the reaction network entirely on the GPU have been prototyped and are being integrated. We are

exploring how to adapt PETSc to support the Jacobian updates on the GPU as well.

- In collaboration with RPI, unstructured mesh capabilities are being designed and implemented in GITR and hPIC, with initial indications of the possibility of significant performance gains.
- Sensitivity analysis and uncertainty quantification studies have been carried out in the F-TRIDYN, hPIC, and GITR. These studies have value both for the individual codes and as the starting point of such studies of planned coupled simulations. UQ studies of the W-H interatomic potential have also been carried out to inform MD simulations.
- Improvements to time stepping in COGENT provide more flexibility as to time steps and initial studies have shown significant performance improvements for certain test cases as we work towards a fully kinetic electron model.

SNAP Potentials on Leadership Computers (PNNL): Previous performance work in LAMMPS had focused on the modified W-He Juslin EAM potential. Now that we have shifted to the machine learning Spectral Neighbor Analysis Method (SNAP) potentials, PNNL has been performing benchmarking and performance enhancement efforts to the SNAP implementation in LAMMPS. The Kokkos-based implementation of SNAP in LAMMPS has been built and tested for the 2000 atom 2J8 and 2J14 test problems on Cray XC40 (Intel Haswell, Cori) and the IBM AC922 (POWER9+V100, Summit) architectures. Performance, the time taken to calculate the SNAP potential for each of the atoms per time step in microseconds, was measured on both machine targets. On Summit, various resource sets were successfully tested in weak (holding the number of atoms updated per GPU constant and increasing the number of GPUs) and strong (equally distributing a fixed number of atoms per GPU and increasing the number of GPUs) scaling modes to establish appropriate use scenarios, as shown in Figure 1. NVPROF analysis of single atom operations executed on a single thread block indicates each thread was using a large number of registers increasing register pressure and degrading the performance.

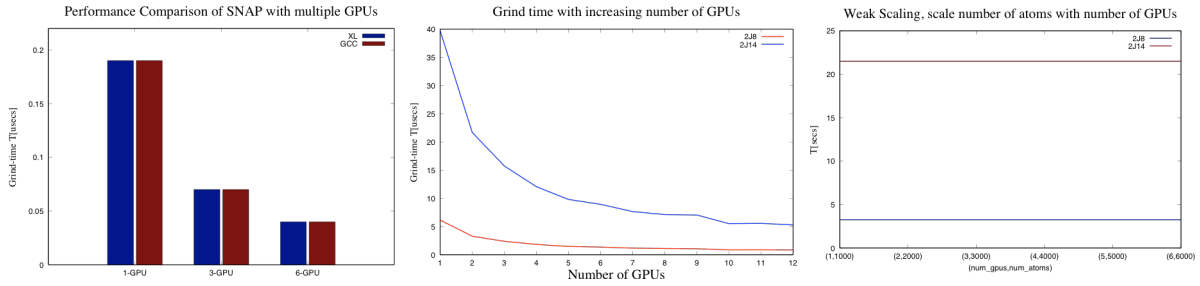

Figure 1. Kokkos backend on Summit. (Left) Single node strong scaling for 2J14 with IBM and GCC compilers. (Center) Strong scaling for both 2J8 and 2J14 on two nodes. (Right) Demonstration of single-node weak scaling for both 2J8 and 2J14.

Porting Xolotl to GPU Accelerators (ORNL): With current and planned HPC systems increasingly relying on GPUs for their computational capability, it has become essential that Xolotl be able to take advantage of GPU hardware. The two primary tools considered for this effort were OpenMP 4.5/5.0 with its GPU offload capability and Kokkos. Kokkos was chosen for several reasons. It provides an abstraction of the parallelism concept and provides support for code to be portable between different hardware configurations and compilers, automatically handling some data layout issues. Kokkos is seeing growing usage. It is supported by the Exascale Computing Project (ECP) and is being used by several ECP applications projects, and its project members have been influential in the evolution of the ISO C++ standard.

Xolotl uses PETSc to solve a non-linear partial differential equation (PDE) on a large number of points with an extremely large number of degrees of freedom. Both the "right hand side" of the PDE and the Jacobian are derived from the reaction network representing the interactions of the different types of clusters modeled in Xolotl. A key to maximizing performance on GPU systems is that the reaction network and Jacobian data structures should be moved between host and device (GPU) memories as little as possible. Thus, our GPU porting strategy has focused on the ability to build and maintain these data structures entirely in GPU memory. Our new plsm (Parallel Lattice Subpaving Map) library implements this strategy using Kokkos, which allows it to be portable across multiple types of GPUs (such ports are being carried out by the Kokkos ECP project) as well as other processor architectures. This library is used to represent the phase space as a region within an N-dimensional lattice, which is then refined according to user-specified rules for refinement, region selection, and subdivision ratio to support grouping strategies to make the reaction network more efficient.

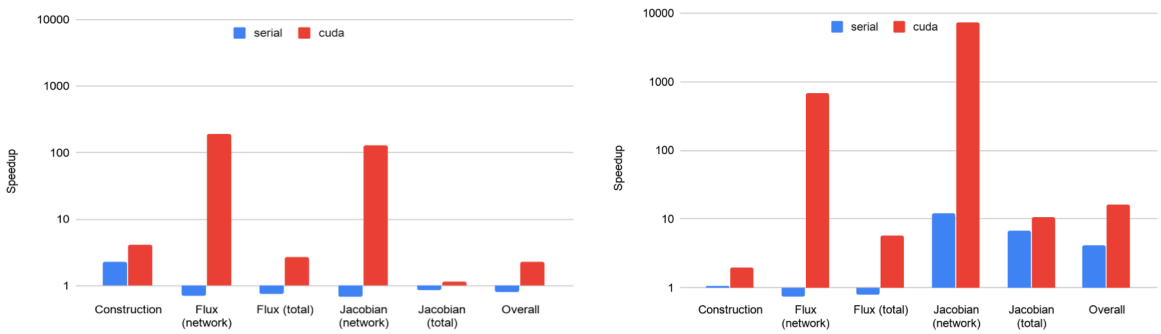

Figure 2. Speedup of Xolotl Kokkos-based port the serial (blue) and CUDA (blue) Kokkos backends compared with current production version. Two test cases are considered: *left*: 9999 DOF representing 9999 clusters with no grouping; *right*: 20079 DOF representing 99999 clusters with grouping.

While continuing to test and tune the plsm library itself, we are now refactoring Xolotl to incorporate the library. Currently, the reaction network can be built, and the right-hand side of the PDE updated entirely on the GPU. PETSc support for GPUs is emerging and incomplete; currently, it does not provide an API for updating the Jacobian matrix entirely on the GPU if that matrix uses a sparse representation (as in Xolotl). With guidance from PETSc developers within the SciDAC FASTMath institute and this project, we recently completed prototype modifications to PETSc that allow us to access and update a PETSc sparse matrix stored in GPU memory, and are currently working to demonstrate their efficacy in updating the Jacobian matrix of a non-linear solve without incurring the cost of transferring matrix data between GPU and host memory. Nevertheless, initial results are promising. Figure 2 shows some early performance results comparing the new plsm-based version of Xolotl with the production version. Timings for the portions of the flux and Jacobian calculations done strictly by the reaction network are distinguished from the total timings for those calculations to differentiate the fully on-GPU computations from those requiring significant data movement. Once comprehensive GPU support becomes available in PETSc, the overall performance is expected to improve further.

Note that the GPU development work in Xolotl is being jointly funded by the *Simulation of Fission Gas in Uranium Oxide Nuclear Fuel* SciDAC-4 project supported by the Office of Nuclear Energy and ASCR, as it is equally relevant to that project.

Enhancing the Visualization Capabilities of Xolotl (ORNL): Our visualization activities over the past year have been focused on supporting the needs of Xolotl. The primary improvement was the creation of a reader in VisIt to read two different types of Xolotl data. This reader reads both 0D and 1D Xolotl data

and allows easy plotting and viewing of different sets of variables. This reader is implemented to read a ".xolotl" file format, and was officially released in VisIt as of VisIt Version 3.1.

Work is in progress to extend the VisIt reader to support visualization of plsm library phase-space. This update will allow new visualizations to be performed that are now needed to help visually verify the properties of the lattice in Xolotl, which will facilitate testing and debugging of the plsm library as well as quality checks on production simulations.

We are also working on implementing VTK-h (for hybrid parallelization) in Xolotl to extend upgrade to VTK-m from older visualization libraries that we carried out last year. The use of VTK-h will allow MPI parallelism for visualization and should increase the speed of visualization operations.

Improving Event Detection and Error Estimation in Xolotl (ANL): Aspects of the cluster dynamics modeled by Xolotl pose challenges for the solvers. As bubbles approach a pre-determined size, they are assigned a random number to determine if they will burst. The bubble-bursting event is handled by the PETSc time stepper (TS) event handler. In general, when a bubble bursts, it will happen between two integrator time steps rather than exactly on a time step. The TS event handler must detect the bursting event and back up the time integrator to specify the time of the event, within a tolerance determined by the error control. It then calls the application code to burst the bubble, which changes the physical parameters of the problem, adjusts the time-step to reflect the much faster dynamics of the bursting bubble, and restarts the time integration at the time of the burst. The original implementation detected the event by locating the time when an indicator function was below a tolerance (i.e., effectively zero). However, our experience was that when the indicator function is very flat, the same event might be detected again immediately when the time stepper is restarted, creating an infinite loop. After analyzing the problem, we concluded that a better approach would be to look for the interval containing the zero crossing of the indicator function to avoid repeated detection. We continue to monitor solver behavior and expect to further tweak that event management algorithm as Xolotl simulations produce more "interesting" dynamics.

Error estimators and controllers for ODEs are performed in floating point numbers and thus care must be taken when numbers of very different scales are used in arithmetic or in making control decisions within the algorithm; for example, to increase or decrease the time-step. Cluster dynamics poses two problems for such estimators and controllers. The first is that because of round-off errors, values of the cluster concentrations may become slightly negative, which is non-physical and can disrupt the solution process. The second problem is that the range of values of the cluster concentrations changes dramatically (many orders of magnitude) from the beginning to the final time-step. Error estimators and time-step controllers traditionally require either that the relative scale of the solution values does not change much over the time interval, or that the scales are known in advance and can be provided in a scaling vector. Xolotl violates both requirements and, unfortunately, the naive approach of just setting extremely small (or negative) values to zero results in incorrect solutions at the final time – the tiny numbers do matter because they accumulate and occasionally get scaled by very large numbers. We have developed several practical approaches to handling the scaling issues, some based on similar problems that appear in combustion computations. Rather than removing tiny numbers we replace them with the smallest physically relevant non-zero numbers during the computation. For example, since it is not physically possible to have 10^{-3} of an atom in a cell one replaces the value 10^{-3} with 1. We have been examining configurations of Xolotl that produce problems with restricting the time-step to non-physical regimes like 10^{-12} seconds, to resolve the problem and keep the time-step constraints within physically reasonable values. So far, for the cases that Xolotl has generated we have been able to adjust the tolerances and small values appropriately. A general theory would be desirable but seems unlikely.

Sensitivity analysis in F-TRIDYN (SNL, UIUC): Global sensitivity analysis (GSA) was extended to F-TRIDYN. Polynomial chaos (PC) surrogates were constructed for the (He on W) sputtering yield as a function of 5 uncertain input parameters (W surface binding energy, and cutoff and displacement energies of W and He), and 2 control parameters (He beam energy and incident angle relative to the W surface). Random samples of these parameters were propagated through F-TRIDYN computations to generate training data for fitting the PC surrogate. GSA using this surrogate resulted in He beam energy and W surface binding energy being identified as the most impactful on sputtering yield. Sensitivity index computations converged quite quickly (Figure 3a). We used samples of these two parameters to build a 2D PC surrogate of sputtering yield over their given ranges (Figure 3b), highlighting associated dependencies in the model.

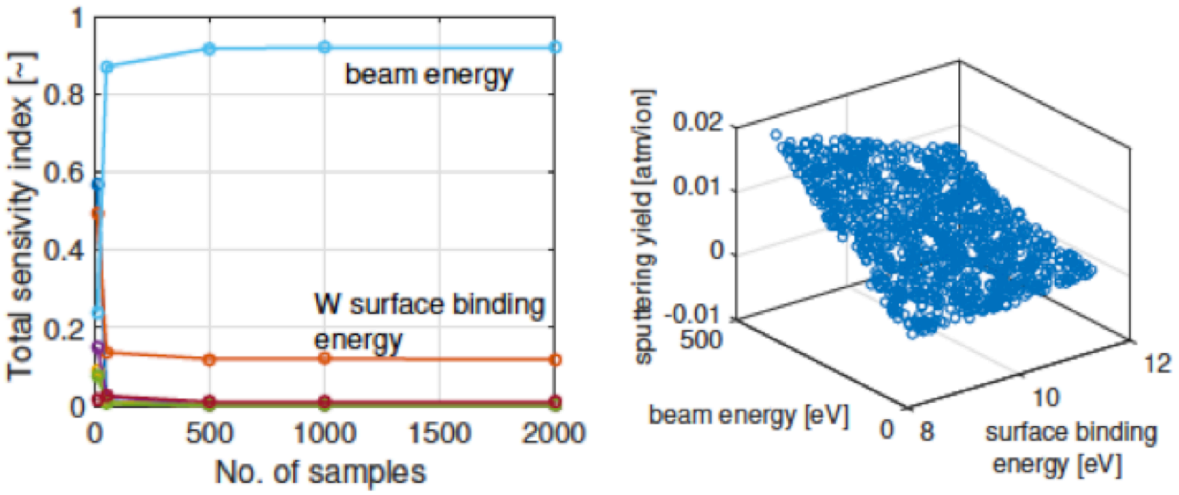

Figure 3. (a) Convergence of the total sensitivity indices with increasing number of FTRIDYN simulations runs, (b) 2D response surface for sputtering yield as a function of W surface binding energy and incident He beam energy.

UQ in GITR (ORNL, SNL): Continuing our UQ work with GITR, we represented uncertain inputs (plasma profiles for temperature and ion flux), previously fitted using Langmuir probe measurements, as random fields parameterized by PC expansions. The joint uncertain representation of temperature and ion flux curves was propagated through GITR to build PC surrogates for two output quantities of interest, namely mass gain of the titania bead tower and emission intensity, for which experimental data is available for validation. Comparisons to this data highlighted a positive bias in the GITR mass gain predictions consistently across all beads in the titania tower. This bias is currently under investigation. GSA results with the current predictions indicate that the ion flux density profile is the main contributor to the output uncertainty.

Unstructured Mesh Support for GITR and hPIC (RPI): Recent work has focused on two primary developments: i) a PUMIPic-based implementation of all physics terms in the GITRm code for global impurity transport, and ii) a multi-block boundary layer (MBBL) mesh capability in PUMIPic for the hPIC code targeting sheath/pre-sheath region simulations. For the GITRm code, efforts included use of PUMIPic-based data parallelism on GPUs and a code-to-code verification between the existing GITR code and the (new) GITRm code. Ongoing efforts include multi-GPU implementation and execution for cases of interest. For the hPIC code, efforts involved development, integration and optimization of all the necessary PUMIPic-MBBL mesh APIs into the hPIC code as well as verification against the standard uniform hPIC code. Further, highly nonuniform MBBL meshes were tested for a large linear plasma device resulting in computational savings up to 100x as compared to the standard uniform hPIC code.

Ongoing efforts are focused on parallelism and tensor product based 2D MBBL meshes. This work is fully reported in RPI's separate annual report.

Uncertainty Quantification in hPIC Simulations (ORNL, UIUC): hPIC simulations rely on the choice of a set of numerical and physical input parameters. The numerical parameters include the number of Debye lengths in the domain; the number of points per Debye length; the number of points per gyroperiod; the number of ion transit times; and the number of particles per cell. The physical parameters include the magnetic field magnitude and angle; the electron and ion temperatures; and the ion mass, charge number, and density. We find that the main numerical parameter contributing to statistical noise is the number of particles per cell. Additionally, the ratio of the electron to ion temperature is the physical parameter most significantly contributing to uncertainty.

We performed a statistical characterization of the noise introduced by the choice of the number of particles per cell and characterized uncertainty resulting from the temperature ratio variation. We also characterized the bias behavior relative to the analytical prediction of the electric potential, ϕ_w. These results allowed us to devise strategies to optimize the computational cost of hPIC simulations, including employing less expensive coarse simulations to inform the statistics of more expensive fine simulations.

Uncertainty Quantification of W-H interatomic potentials (LANL): A major goal in this UQ effort is to quantify uncertainties in MD models due to the interatomic potential function. Often, fitted potentials in the literature are inconsistent with high quality DFT realizations for new structures. The past and current UQ work includes obtaining a probabilistic potential constraining the W-H and H-H potential interaction to the DFT output; the metric of the forces on H are used here. This can be extended to include He and other interactions. The Tersoff parameterization following Juslin (2005) and the EAM potential in Wang et al (2017) were considered in the development of a probabilistic potential. The DFT output in this work are paths of a migration process of H atoms on a (111) surface of W, as well as many structures of multiple H atoms within bulk W. For the 12 parameter EAM potential, 1000 initial design points were narrowed to 569 after eliminating non-physical parameter combinations that result in MD model failures. The EAM potential seems to provide a fit as good or better than the Tersoff potential for the bulk DFT structures; with R^2 values of 0.9138 and 0.8633 for EAM and Tersoff respectively. The surface DFT structures do not seem to constrain EAM as well as the Tersoff potential. Future work includes developing a sequential design approach to select new DFT structures and implementing UQ approaches for SNAP potentials.

Improved Time Integration for COGENT (LLNL): The need for a fully kinetic electron model to enable higher-fidelity heat flux predictions continues to drive COGENT development. The challenge of including a fully kinetic electron model lies in the extremely short time scales required to capture the dynamics of electrons, plasma waves and shear Alfven waves, and is greatly facilitated by the implicit time integration of electron advection.

In previous versions of COGENT, an implicit-explicit (IMEX) framework was implemented to solve the collisional Vlasov equation with implicit integration of the collisional term[1]. To meet the needs of the PSI SciDAC, we have now extended it to a more flexible framework that allows user-input-based partitioning of the overall dynamics into implicitly and explicitly integrated components. The governing system of equations is integrated using high-order, conservative, multistage Additive Runge-Kutta (ARK) methods, and the Jacobian-free Newton-Krylov (JFNK) method is used to solve the nonlinear system of equations at each stage. The efficiency of this approach depends upon the implementation of efficient pre-conditioners, and, in order to address this need, we have developed an operator-split-based multiphysics pre-conditioner that provides efficient pre-conditioners for each of the implicit dynamical operators

[1] D. Ghosh, M.A. Dorf, M.R. Dorr, and J. Hittinger, *J. Sc. Comput.*, **77** (2018) 819-849.

independently. This allows us to design and implement a pre-conditioner for each implicit dynamical operator that exploits its own particular features. When treating an advection operator implicitly, we take advantage of the recently developed approximate ideal restriction (AIR) based algebraic multigrid (AMG) algorithms that extend the effectiveness of AMG methods to asymmetric advective operators.

Using this new capability, we have been investigating the optimal combination of various solver parameters on a neoclassical transport problem in which both advection and collisions are declared as implicit in the framework, as will be shown in the Task 3 results describing an ELM heat pulse. Key solution metrics are in close agreement, even when using time steps 40 times larger than that required for explicit time integration. An order of magnitude improvement in the overall wall clock speedup has also been observed.

Task 1. PFC Surface Response (Scale-bridging to extend capability of Xolotl PFC Simulator)
Our approach to modeling the divertor surface response is based on simultaneously attacking this problem from both a "bottom-up" atomistic-based approach, as well as from a "top-down" continuum-scale perspective that focuses on kinetic models of species reactions and diffusion. This simultaneous approach to multiscale materials modeling improves the prospects for scale bridging, or multiscale integration, and is imperative to predict PFC performance with complex, inherently multiscale materials degradation and mixed material formation. This simultaneous approach ensures that we utilize atomistic modeling for the discovery science required to identify key phenomena and mechanisms that we can coarse grain for implementation into our cluster dynamics simulator and reduced-order models of tungsten surface evolution upon exposure to burning plasma conditions involving a number of impurity elements including beryllium and nitrogen. Within Task 1, we would also like to note our engagement with researchers at UCLA, where the focus of their work is on the interface between bulk radiation damage and near-surface plasma surface interactions. A brief summary of their work is included here, but will be more fully reported in their own annual FES progress report.

Summary of Accomplishments (May 2019-April 2020):

• Initiated development of machine learning, SNAP interatomic potential for W-N;
• Identified the atomistic mechanisms responsible for reduced H permeation through a helium bubble layer near the plasma-exposed surface of tungsten;
• Quantified the impact of helium implantation (bubble formation) and temperature on the elastic moduli of helium plasma-exposed tungsten;
• Initiated atomistic MD simulations to discover the impact of helium clusters on dislocation and grain boundary mobility in tungsten;
• Successfully validated an atomistically-informed stochastic cluster dynamics model of the influence of radiation damage on deuterium thermal desorption in tungsten;
• Extended the experimentally validated continuum-scale surface evolution model for helium plasma-exposed tungsten to evaluate the influence of exposure temperature; and
• Performed targeted experiments on PISCES-A to evaluate sub-surface material transport during helium plasma exposure.

W-N interatomic potential development (SNL, UTK): To extend the existing tungsten SNAP potential for evaluating the impact of nitrogen, introduced as a radiative divertor gas, on plasma surface interactions of tungsten, additional training data for both nitrogen and mixed tungsten-nitrogen configurations are needed. A potential for studying nitrogen implantation in tungsten and the subsequent formation of tungsten nitrides will need to accurately reproduce nitrogen gas properties, the adsorption/desorption of nitrogen on tungsten surfaces, and the diffusion and trapping of nitrogen in the tungsten bulk. For pure nitrogen, the nitrogen dimer and trimer binding curves as well as random distributions of nitrogen molecules at various densities were generated as training data. The mixed W-N training data included

both bulk configurations of nitrogen defects in tungsten and expected tungsten nitrides (W_xN_x) as well as atomic and molecular nitrogen surface adsorption and diffusion on and into a tungsten surface. The total W-N training set includes ~35,000 configurations.

SNAP has successfully been used to model metallic systems but has yet to be used to develop potentials for gases. Training data for gases is sparse compared to the typical metallic periodic systems and SNAP will need to be able to accurately reproduce nitrogen dimers as the most stable form of nitrogen in dynamic simulations. While empirical potentials ensure by construction the correct nitrogen dimer binding, while preventing the formation of larger clusters, the machine learning SNAP potential 'learns' such behavior by training on suitable atomic configurations. Therefore, potentials were initially fit for just nitrogen to test whether SNAP could reproduce the expected behavior of nitrogen gas. Potentials were fit using DAKOTA and the nitrogen dimer and trimer binding curves were targeted as objective functions. SNAP successfully reproduced the predicted dimer and trimer binding energies from DFT as shown in Figure 4a. An additional simulation outside of the fitting dataset was performed to test the predicted dynamical behavior. Early potentials had reproduced the dimer and trimer binding energies but the formation of larger nitrogen clusters was observed in MD simulations. Therefore, a box of nitrogen dimers was initiated and run for 10 ps at 1000 K. Figure 4b shows the initial configuration of N_2 molecules at t=0 ps. At t=10ps (Figure 4c) all of the dimers remain intact and no larger clusters are formed.

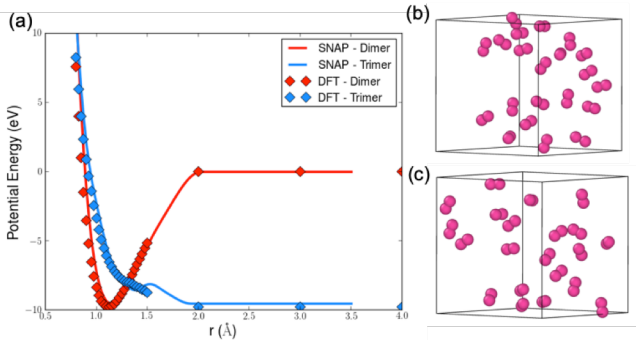

Figure 4. (a) Nitrogen dimer (red) and trimer (blue) binding curves predicted by SNAP (line) and DFT (diamonds). Atomistic snapshots of nitrogen dimers at 1000 K at (b) 0 ps and (c) 10 ps.

The next step for generating the full W-N potential is reintroduction of W and W-N training data. The hyper-parameters and group weights for the pure nitrogen fitting that produced successful results were carried into the full W-N fit. Currently, we are fitting the full W-N potential to a DFT database with the addition of objective functions targeting cohesive energies for the tungsten nitrides, the defect formation energies for nitrogen in bulk tungsten, and the adsorption energies for both atomic and molecular nitrogen. Once a potential is fit for W-N we can then begin to perform MD simulations of nitrogen implantation in tungsten to study nitrogen diffusion, trapping, and nitride formation in tungsten.

MD simulation results of W-Be-He (SNL): We have extended our previous simulations of beryllium implantation in tungsten using SNAP potentials to include helium. This includes the development of a new Be-He pair potential. To investigate the impact of mixed W-Be surface layers on helium implantation, we performed helium implantation in pristine tungsten, the C14 WBe_2 intermetallic structure, and a beryllium-exposed tungsten structure generated previously. The presence of beryllium greatly modifies the initial implantation and further helium diffusion and helium bubble nucleation. Figure 5 depicts the simulations at a helium fluence of 2.8×10^{19} He/m^2 for (a) pristine tungsten, (b) C14 intermetallic, and (c) beryllium-implanted tungsten. In the cases where beryllium is present, the helium resides much closer to the surface. About 80% of the helium is within the first 2 nm as opposed to only 40% in pure tungsten. The He retention is also significantly higher for the surfaces incorporating beryllium, with 49% for C14 and 67% for beryllium implantation, compared to 37% in pristine tungsten. In addition, the helium cluster size distribution is also skewed towards smaller clusters with a higher number of clusters when beryllium is present; these observations are consistent with a reduction in the

helium diffusivity. The largest size clusters in either surface incorporating beryllium are around 15 helium atoms while clusters of up to size 30 are present in pure tungsten.

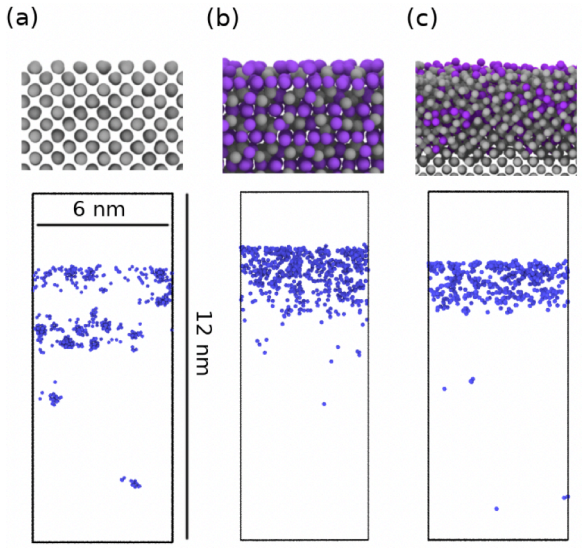

Figure 5. Atomistic snapshots of the cumulative helium implantation at 1000K and ~3×10^{19} m^{-2} for (a) pure tungsten, (b) C14 WBe_2 Laves phase, and (c) an amorphous mixed W-Be layer formed by prior Be implantation. In each case, the top images depict a cross section of the atomic layers closest to the surface, while the bottom images display the helium atomic positions. Grey, purple and blue spheres represent tungsten, beryllium and helium atoms, respectively.

The differences in helium behavior between the materials is linked to differences in material properties between tungsten and the mixed materials. The helium diffusion coefficient was found to be two orders of magnitude lower at the simulation temperature of 1000 K in the C14 intermetallic compared to tungsten, and the beryllium vacancy formation energy in C14 was about half that of the tungsten vacancy in either C14 or pure tungsten. The slower diffusion indicates that the helium cannot diffuse either to the surface and desorb or diffuse deeper below the surface, leading to the higher retention and shallower depth distribution in the beryllium containing surfaces. The combined slower diffusion and lower vacancy formation energy results in smaller helium clusters since the threshold for trap mutation is lower since it is easier to displace a beryllium atom to form a He-V complex. This implies that the presence of beryllium at the divertor surface may impact the initial stages of helium bubble nucleation and growth, which is linked to fuzz formation. It is possible that the W-Be intermetallic may slow or even prevent the growth of fuzz. Future large-scale MD modeling will assess the impact of mixed W-Be layers at larger time and length scales needed to understand the effects on helium implantation over time.

H interaction and permeation through He cluster sub-surface layer (UTK, UMissouri): MD simulations have investigated the complex He-H interactions indicated by both experimental and computational studies. The simulations were designed to determine the effect of a helium bubble layer on hydrogen diffusion and permeation. The MD simulations also compare two sets of interatomic potentials (Wang EAM and Juslin Tersoff potentials) that describe the W-W, W-H, and H-H interactions. The Wang EAM potential predicts ~10x higher hydrogen diffusion rates and ~5x higher H surface concentrations. Both potentials predict that pre-existing He-V clusters significantly reduce H permeation and impact hydrogen diffusion. Reduced H diffusion and permeation results from two effects, namely, trapping of hydrogen to He-V clusters and the impact of an approximately biaxial stress state in the W matrix induced by the presence of the high-pressure helium bubbles. The binding energy of hydrogen to selected He-V clusters was quantified by molecular statics calculations using these two interatomic potentials, as well as DFT, and the resulting values were calculated to be between 0.6 and 1.2 eV, with precise values dependent on the interatomic potential and cluster size. The high-pressure helium bubbles in the pre-existing helium implanted W slab were shown to induce an approximately biaxial compressive stress state. Static nudged-elastic band (NEB) calculations were performed to assess H activation energy for diffusion, in which the approximately bi-axial compressive stress states increased the activation energy for migration vertically through the tungsten layers and decreased the barrier for lateral motion. Overall, these trapping and stress-

induced effects of high-pressure helium bubbles reduce the diffusion and permeation of hydrogen through the tungsten slab when compared to a pure tungsten slab with no pre-existing damage.

H implantation into W (UMissouri): Large-scale MD simulations of hydrogen implantation into tungsten have been continuing, although these simulations are more challenging than prior work on helium due to the chemical bonding and hydrogen bonding. The deuterium simulations were performed on several surface orientations of single crystalline tungsten at 933 K—the same temperature used in other simulations involving helium—using the same direct implantation technique that has been successful for helium studies. Several major differences are apparent with hydrogen compared to helium. For one, helium undergoes self-clustering, but hydrogen does not do so, and in fact hydrogen atoms within the metal repel one another. Even with vacancies added at the start of the simulation, the only clusters of hydrogen observed were of 5–6 atoms in size bound to the vacancy; at higher fluence, this hydrogen–vacancy cluster complex repels other dissolved hydrogen just as interstitial hydrogen does. These results are consistent with density functional theory calculations[2], which also concluded that the interaction between two interstitial hydrogen atoms in tungsten is repulsive. This effect persists in the MD simulations even at a relatively high temperature. Figure 6 plots the deuterium depth distribution over time, which tends to follow the same qualitative trend as was present in the initial depth profiles, except stretched deeper, until the profile encountered the bottom of the super-cell.

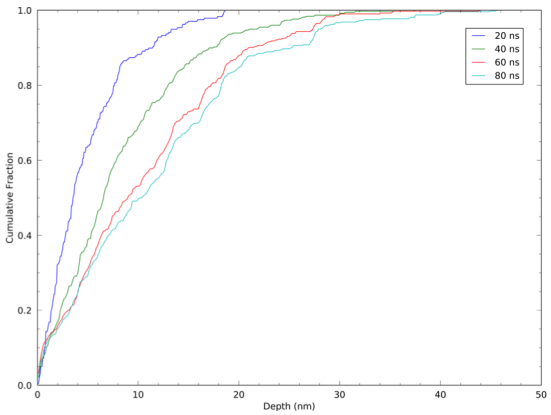

Figure 6. Evolution of (cumulative) depth distributionof implanted deuterium beneath a W (100) surface with a nominal implantation flux of 2.5×10^{26} $m^{-2}s^{-1}$, as a function of time. The tungsten slab is 50 nm thick, and the deepest D atom is located ~44 nm below the surface at 80 ns.

The complete lack of deuterium clustering that might lead to blistering has prompted us to seek alternative explanations for the experimentally observed hydrogen-induced blistering. An experimental study performed by Balden, et. al.[3] on polycrystalline tungsten exposed to deuterium plasma appears to show that a blister forms by delamination at grain boundaries. This work has motivated new large-scale MD simulations and molecular statics investigation of the partitioning of hydrogen to grain boundaries, which are underway. A study of the energy required to separate two grains, with and without hydrogen present, is ongoing. This work will proceed on three fronts: (1) continue large-scale MD simulations, implanting at reasonable fluxes; (2) perform targeted, smaller MD simulations with much higher implantation rates, with implantation directly to the grain boundary so as to *force* a high concentration of hydrogen there; and (3) perform controlled yield strength tests of hydrogen-laden grain boundaries to determine whether blister formation might be induced by external forces, rather than by hydrogen pressure alone.

Diffusion of small, over-pressurized He bubbles in W (LANL): Ongoing MD simulations are being used to investigate the diffusion mechanisms of over-pressurized He bubbles in W, which occur via Frenkel pair nucleation, self-interstitial atom (SIA) migration, and Frenkel pair annihilation. This information is crucial for larger scale models, such as Xolotl, to enhance fidelity in connecting to experimental conditions. Bubble migration is expected to be a slow process, so initially, the migration at high temperature (1200-2000 K), of highly over-pressurized bubbles (4.5-7 He/V) was studied with MD. In

[2] L.-F. Wang, X. Shu, G.-H. Lu, and F. Gao, *Journal of Physics: Condensed Matter* **29** (2017) 435401.
[3] M. Balden, S. Lindig, A. Manhard, and J.-H. You, *Journal of Nuclear Materials* **414** (2011) 69–72.

these simulations, various initial vacancy clusters, ranging from 1 to 6 in size, were populated with differing amounts of He. As the simulations proceed, these bubbles evolve as they nucleate and annihilate Frenkel pairs based on the amount of He contained and the number of existing SIAs on the bubble surface. After 5 ns of simulation, these bubbles have relaxed to a state that typically contains 3-7 vacancies with satellite SIAs. To gain insight into the diffusion of these bubbles, we record the nucleation and annihilation rates as a function of temperature and He content as well as the diffusivity of the SIAs that form and persist at the periphery of the bubbles. It is found that bubbles are most mobile when the nucleation/annihilation rates of Frenkel pairs are nearly equal and when the bubbles are less than 0.36 nm in diameter with He/V ratios greater than 6. SIAs are found to be highly mobile and strongly impact the nucleation/annihilation rates and cluster evolution. This information will help inform a novel model of bubble diffusion that accounts for Frenkel Pair nucleation and annihilation rates as well as the diffusivity of satellite SIAs. An initial version of the model suggests 2 regimes of bubble diffusion: a R^{-2} regime for small bubbles in which nucleated interstitials can diffuse to any point on the bubble periphery before annihilation, and a R^{-4} regime for larger bubbles in which interstitials do not travel far from the point of nucleation before annihilation. Future simulations will focus on lower temperature and pressure bubbles, which have decreased Frenkel pair nucleation/annihilation rates, and will be studied with accelerated MD techniques, such as ParSplice, to extend the temporal domain of the simulations.

Elastic properties of plasma-exposed tungsten (UMass, UTK): We have performed systematic molecular-dynamics computations of the elastic properties of single-crystalline tungsten containing regular periodic arrangements of structural defects, voids and over-pressurized He nano-bubbles, related to plasma exposure of PFC tungsten in nuclear fusion devices. Our computations reveal that the empty voids are centers of dilatation resulting in development of tensile stress in the tungsten matrix, whereas He-filled voids (nano-bubbles) introduce compressive stress in the plasma-exposed tungsten. We find that the dependence of the elastic moduli of plasma-exposed tungsten, namely, the bulk, Young, and shear modulus, on its void fraction follows a universal exponential scaling relation. We also find that the elastic moduli of plasma-exposed tungsten soften substantially as a function of He content in the tungsten matrix, following an exponential scaling relation; this He-induced exponential softening is in addition to the softening caused in the matrix with increasing temperature. A systematic characterization of the dependence of the elastic moduli on the He bubble size reveals that He bubble growth affects significantly both the bulk modulus and the Poisson ratio of plasma-exposed tungsten, while its effect on the Young and shear moduli of the plasma-exposed material is weak. Figure 7 shows representative results for the dependence of the bulk modulus, K, of PFC tungsten (scaled with the bulk modulus of perfect BCC tungsten at the same temperature, K_0) as a function of the volume fraction of He bubbles (porosity, ϕ) and of the He content in the tungsten matrix (expressed as atomic percentage).

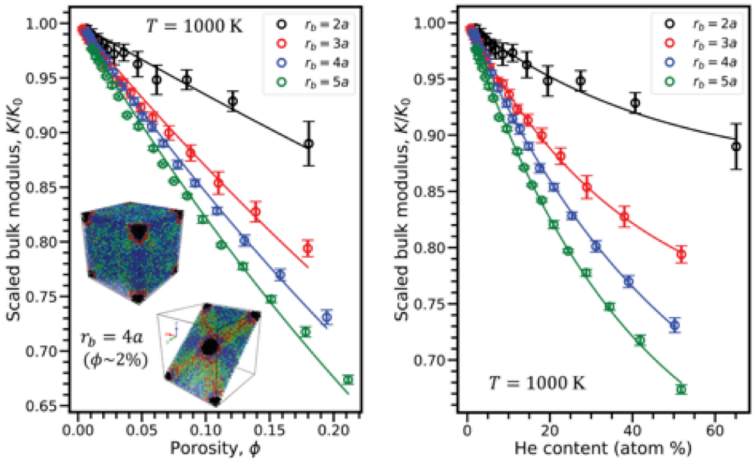

Figure 7. Dependence of scaled bulk modulus, K/K_0, of PFC tungsten on He bubble volume fraction (left) and He content (right); the solid lines represent optimal fits to each dataset according to exponential scaling relations. The insets in the plot on the left show representative atomic-level pressure distributions in the tungsten matrix.

Having established that the elastic properties of PFC tungsten depend on the volume fraction of He-filled bubbles in the tungsten matrix and the He bubble size, we expect that the scaling relations derived for the elastic moduli as a function of porosity and bubble size will be valid for the actual near-surface

region of plasma-exposed tungsten, which contains spatially random distributions of irregularly shaped bubbles with a narrow size distribution. Specifically, we expect our findings based on a regular bubble array in tungsten to be in semi-quantitative agreement with the elastic properties of actual PFC tungsten to within the statistical errors related to the actual bubble size and spatial distribution. Our findings contribute significantly to our fundamental understanding of the mechanical response of PFC materials upon plasma exposure as well as to the development of a structure-properties database in support of predictive modeling of the dynamical response of PFCs in nuclear fusion devices.

Effect of H/He/Interstitial clusters on the motion of dislocations and grain boundaries (LANL): The motion of dislocations and grain boundaries (GBs) control the processes of recovery and recrystallization in polycrystalline W. The presence of radiation-induced damage significantly affects the mobility of these line and areal defects and, consequently the recovery and recrystallization processes. A key focus is to understand the interactions between these different kinds of defects, especially related to He and H-containing bubbles or defect clusters. A combination of MD and a novel parallel replica dynamics (Koopman ParRep) has been used to investigate the effect of small He clusters (He_3V) on the mobility of edge dislocations in W. In Koopman-ParRep, states and transitions are identified *on-the-fly* using a diffusion distance metric calculated from an approximation of the Koopman dynamics operator. The

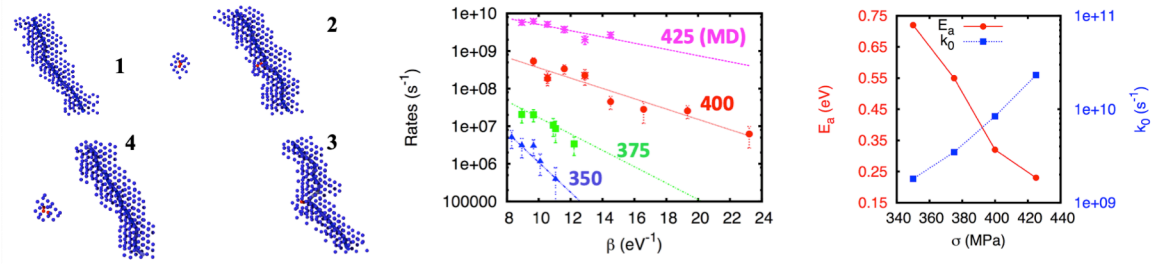

Figure 8. Different stages of edge dislocation – He3V interaction (left) as detected on-the-fly by Koopman ParRep. Rates of edge dislocation bypass (center) of the He3V cluster at different applied stress levels (MPa). Pre-factors and activation energies (right) for the dislocation bypass mechanism as a function of applied stress.

Koopman-ParRep simulations are fully integrated with LAMMPS and have been scaled up to 600 replicas, enabling μs-long simulations. Figure 8 shows representative results from this study. The predicted rates for bypass, in the range 350-425 MPa, show a strong dependence on the applied stress and spans ~4 orders of magnitude. Note that the lattice friction is <20 MPa for the edge dislocation. The results predict that these small clusters behave as strong obstacles to dislocation glide, given the spacing (≈9 nm) along the dislocation line in our simulations. The simulations do not predict Orowan looping; instead, part of the dislocation line climbs in order to overcome the obstacle, reminiscent of the Hirsch mechanism. We are currently collecting more data in order to fit these computational predictions using a Kock's model for the interaction rates.

We are also studying the effect of H and He interstitials on shear-coupled motion of <100> and <110> symmetric tilt GBs in W at temperatures ranging from 1000 to 2000 K. We have investigated this process in four GBs: Σ13<100>{023}, Σ85<100>{067}, Σ33<110>{118}, Σ13<110>{332}. These boundaries have critical stresses (for shear-coupled motion at 0 K) ranging from 80 MPa to 3 GPa. Figure 9 shows the structure of these boundaries at 1000 K when loaded with 0.01 He/Å^2.

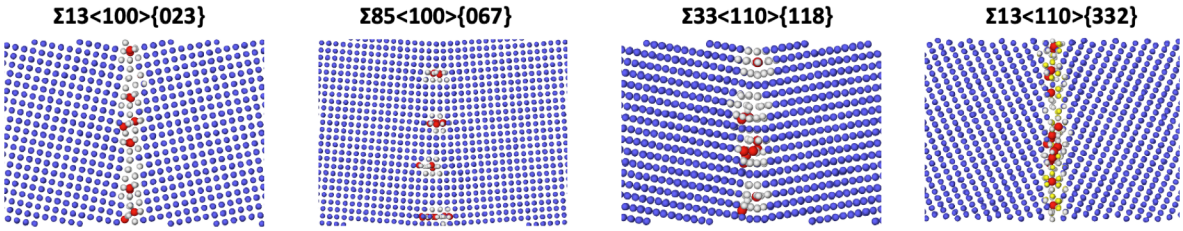

Figure 9. Structure of selected <110> and <111> symmetric tilt grain boundaries in W, which exhibit shear coupled motion. The dark red spheres represent He interstitials, while blue spheres are BCC tungsten, yellow spheres are HCP tungsten and white spheres are disordered tungsten atoms.

Our simulations predict that presence of interstitial H at 0.01 H/Å^2 produces significant pinning effects on these GBs and hinders both shearing and normal motion of the GBs. Presence of interstitial He at the same concentration results in a more complex behavior where, in some GBs such as Σ13<100>{023}, only the normal (i.e., the coupled) motion is suppressed but shearing still occurs. This behavior can have important consequences for retarding recrystallization, as shear-coupled normal motion is a significant component of GB mobility. We are currently investigating the origins of this effect. A study of the effect of He/H on the kinetics of shear-coupled motion is also underway.

KMC modeling of radiation damage and sub-surface helium evolution in W (PNNL): The first part of this task is to perform He irradiation accumulation in sub-surface W using an object kinetic Monte Carlo (OKMC) technique. The aim is to evolve He bubble and cluster microstructure under experimentally relevant fluxes and fluences. In this report period, the benchmarking of OKMC simulations, performed using the KSOME code[4], to large-scale MD simulations has been extended to include the effect of depth-dependent trap mutation for the W (100) surface. For this, the trap mutation kinetics as a function of cluster size and depth has been calculated based on a database of relative probabilities of trap mutation events from MD simulations. Figure 10 shows a comparison of the depth profile of the cumulative fraction of retained He between KMC and large-scale MD simulations. The results of the KMC simulation without taking into account the depth-dependent trap mutation are also shown. The key finding is that accounting for the depth-dependent trap mutation results in a characteristic "kink" in the depth profile near the surface, consistent with that in the large-scale MD simulations. The kink implies a He-depleted region in between near-surface and deeper regions. This is a consequence of a combination of elastic attraction of He clusters toward the surface and the fact that the probability for trap mutation increases near the surface compared to the bulk. This effect is stronger for lower fluxes presumably because smaller clusters are more mobile and able to contribute more than larger clusters. Overall, this produces a higher fraction of retained He near the surface

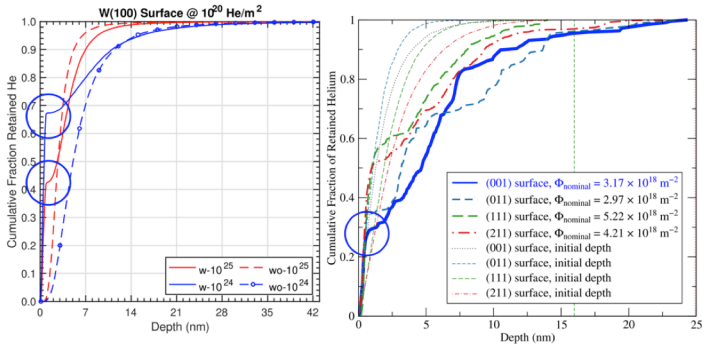

(a) KMC (b) MD

Figure 10. Cumulative fraction of retained He as a function of depth in W100 surface (a) KMC results with 10^{24} and 10^{25} He/m^{2}s fluxes and at 10^{20} He/m^2 fluence. *w (solid lines)* and *wo (dashed lines)* correspond to with and without accounting for depth-dependent trap mutations, (b) MD data with 4 $\times 10^{25}$He m^{-2}s^{-1} flux and at 3.17$\times 10^{18}$ He m^{-2} fluence.

[4] G. Nandipati, W. Setyawan, H. L. Heinisch, K. J. Roche, R. J. Kurtz, B. D. Wirth, *J. Nucl. Mater.* **462** (2015) 338-344.

(corresponding to the kink) and a wider depletion region for lower fluxes. The comparison with the MD results is encouraging. Nevertheless, given that the MD flux is between the two KMC fluxes, the MD kink should be located also in between the KMC kinks, but this is not the case yet. Work is on-going to empirically adjust the formula for capture radii to better optimize the KMC parameters before long-time simulations could be performed. Comparison with XOLOTL results will also be performed.

The second part of this task is to perform radiation damage accumulation in bulk W subjected to 14-MeV neutrons. The damage accumulation is simulated as a function of flux and impurity concentration. The influence of diffusion dimensionality of self-interstitial atom (SIA) clusters (1D, 3D, and confined-1D) is explored. Interestingly, the confined-1D case, where the SIA clusters diffuse in 1D and are repeatedly trapped/released between two impurities (hence confined), produces the lowest amount of damage. Conventionally, the 3D diffusion is expected to produce the lowest extent of damage presumably due to the larger diffusion region accessible for SIA-vacancy recombination.

Sstochastic cluster dynamics modeling of radiation damage influence on D desorption (UCLA, UCSD, UTK): The stochastic cluster dynamics (SCD) method is a mesoscale modeling technique designed as a stochastic variant of mean-field rate theory based on ODE systems. SCD is capable of simulating the microstructure evolution of multispecies systems (vacancies, SIAs, He, H, Re, etc) by dynamically building and sampling the coefficient matrices of the system using the residence-time algorithm. Currently, SCD has been extended to PDE systems that include spatial resolution, allowing the study of the near surface region of first-wall materials exposed to fusion plasmas. As such, this spatially resolved SCD (SR-SCD) naturally captures spatio-temporal fluctuations in the species concentration, which can directly be compared to experimental data. As well, SCD can statistically capture the end tail of the cluster size distributions, which are notoriously difficult to converge in deterministic calculations. At present, SR-SCD is able to simulate up to 1 dpa of accumulated fluence in irradiated materials.

We have recently applied SR-SCD to the study of fuel trapping in damage-implanted W surfaces, i.e. the accumulation of V-H clusters in H-exposed, ion-irradiated W specimens. In collaboration with the UCSD-PISCES group, we have simulated a three-stage experimental process including (i) Cu-ion irradiation of W samples with energies of 3.4 MeV up to 2.2 dpa, (ii) exposure of implanted materials to D_2 plasmas for 2000 s, and (iii) thermal desorption measurements (TDS) of the D-loaded samples. All the boundary conditions were set in accordance with experimentally measured parameters. All model parameters are obtained via detailed atomistic simulations (DFT and semiempirical potentials). Irradiation damage from Cu-ion beam experiments is modeled by a combination of SRIM calculations to obtain spatially-dependent PKA distributions and cascade databases from state-of-the-art MD simulations. Hydrogen exposure is treated as a generalized diffusion problem solved with SR-SCD in the presence of irradiation defects from the prior stage. This results in the formation of hydrogen-vacancy clusters at various depths within the W material. A novel feature of the model is the inclusion of the so-called 'super abundant vacancy mechanism' (akin to trap-mutation in He-exposed metals), by which H-V clusters can grow intrinsically by emission of a single interstitial atom and subsequently absorb more hydrogen atoms. Finally, after a cool-off period, TDS is simulated by SR-SCD as well considering thermal dissociation processes alone. Figure 11 shows a comparison between the simulated and experimental thermal desorption spectra. The simulated peak at

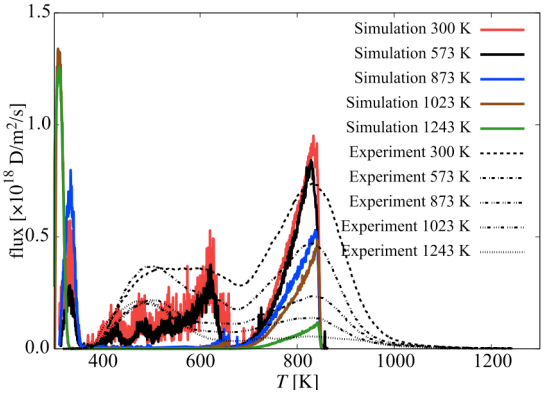

Figure 11. Simulated and experimental thermal desorption spectrum of deuterium from Cu ion implanted tungsten with subsequent D_2 plasma exposure in PISCES-A.

300 K is due to H-trapping by dislocations, which is thought to occur with smaller de-trapping energies (at lower temperatures) than those predicted numerically.

Results from SR-SCD can be used to verify higher scale predictions by Xolotl at shorter time scales and higher physical resolution.

Xolotl enhancements for scale bridging simulations to predict ITER plasma surface interactions and compare to experiments (UTK, ORNL): Xolotl has the capability to model the material surface evolution by tracking the tungsten self-interstial atoms that diffuse to the surface and become adatoms as well as accounting for the effect of tungsten sputtering by plasma ions. The grid defined in Xolotl uses a finer spacing near the surface to better model the sharp changes in implantation profiles and near-surface specific phenomena (bias drift and trap mutation of small helium clusters), and this grid becomes much coarser deeper into the tungsten to allow for simulating a large slab of material. In the current implementation of the evolving surface the spacing of the grid is constant with time and the actual location of the surface moves from point to point on the grid. This implies that in the case of a high sputtering yield, the spacing of the grid near the surface location will become coarser and coarser as the surface position moves deeper and deeper, and near surface phenomena will not be accounted for as accurately. To alleviate this issue, a dynamic (adaptive) grid has been implemented in Xolotl where the near surface grid spacing moves with the surface location while keeping an adequate total length of the material slab. The effect of more accurately modeling the near-surface physics in case of large sputtering yields is currently under evaluation using an experiment performed in PISCES under 250 eV He (above the sputtering threshold).

Continuum-scale modeling of surface morphological evolution of PFC tungsten (UMass, UTK): We have developed an atomistically-informed continuous-domain model, which is the outcome of a hierarchical multiscale modeling strategy over disparate spatiotemporal scales, for simulating surface morphological response and the onset of fuzz formation in He plasma-irradiated tungsten below the sputtering threshold[5]. The model accounts for the development of stress in the He-implanted tungsten layer due to formation of over-pressurized He bubbles in the layer, with large-scale MD simulation results used to

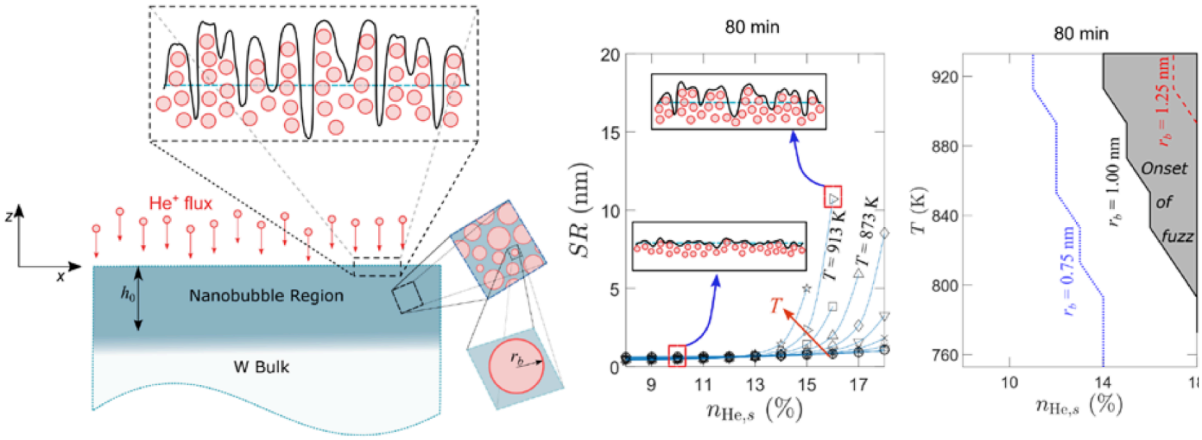

Figure 12. Schematic representation of continuum-scale surface morphological evolution model and predictions of the surface morphological response of PFC tungsten demonstrating nanotendril growth and its dependence on temperature, steady-state He content ($n_{He,s}$), and He bubble size (r_b denotes average bubble radius at steady state)[6].

[5] D. Dasgupta, R.D. Kolasinski, R.W. Friddle, L. Du, D. Maroudas, and B.D. Wirth, *Nuclear Fusion* **59** (2019) 086057.

parameterize the corresponding constitutive equations. Based on this model, we have conducted self-consistent numerical simulations of the He-implanted tungsten surface morphological evolution and compared the simulation results with experimental measurements, which validated the model.

A critical aspect of PFCs is their response to fluctuating heat loads, which can have a significant effect on fuzz formation. We have conducted a systematic study of the PFC tungsten surface morphological response over a temperature range between 753 K and 933 K, aimed at a fundamental understanding of the temperature dependence of fuzz formation, under conditions similar to those at the divertor of fusion reactors. Temperature influences the onset of fuzz formation through the strongly temperature-dependent pressure of subsurface helium bubbles formed by implantation and surface diffusivity of tungsten, in addition to the thermal softening of the elastic moduli of tungsten. We have explored the effects of helium concentration in the implanted tungsten and of average helium bubble size, constructed surface response diagrams predicted over the above temperature range, and interpreted the trends exhibited in such diagrams by computing how all of the relevant parameters (temperature, steady-state He content, and He bubble size) affect the characteristic time scale for surface morphological evolution of PFC tungsten. Representative results over the range of parameters explored are shown in Figure 12. Our findings elucidate the role of plasma exposure duration in fuzz growth and demonstrate the possibility of fuzz formation at temperatures well below the range explored in experimental studies (900 – 2000 K)[6].

Improved wall retention models (UCSD): In collaboration with the UCSD PISCES group, the retention and release of hydrogen isotopes from W-D co-deposited layers was studied to improve understanding and ability to predict the in-vessel inventory in future fusion devices that may utilize tungsten. The release of deuterium from sputter magnetron produced tungsten co-deposit layers was investigated by thermal desorption mass spectrometry and modeled with the reaction-diffusion code FACE. Layers up to ~2 μm thickness, produced at substrate deposition temperatures up to 513 K were modeled. The simulations, utilizing a quasi-continuous distribution of trap energies, show discreteness in trapping sites above ~ 1.5 eV, but smoothness in the distribution below, as shown in Figure 13. The resulting distributions of the de-trapping energies indicate a quasi-exponential decrease in trap concentration with the energy. The increased deposition temperature leads to a systematic loss of trapping in low energy traps and facilitates a moderate increase in trapping in higher energy traps. This indicates that deuterium trapping in the tungsten co-deposits is strongly governed by the temperature of the substrate compared to other influences. In terms of predictive capability, the developed tungsten co-deposit model accurately reproduced changes in desorption heating rate and gave reasonable agreement with predictions for different layer thicknesses and deposition temperatures. The measured D/W ratios in the co-deposit layers were also found to agree reasonably well with predicted scaling laws in the literature.

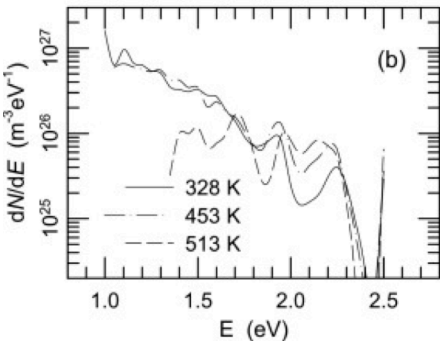

Figure 13. Simulated distribution of de-trapping energies in W-D co-deposits resulting from deposition at different temperatures.

Experimental investigation of material transport and fuzz formation under He plasma exposure (UCSD): Material transport during formation of He-induced nanobubbles and fuzz in W and Mo was investigated for a range of He exposure conditions. In the first experiment, thin films (~48 nm) of W were deposited on Mo substrates by magnetron sputtering deposition. Samples were then exposed to a He plasma in the PISCES-A device at a range of sample temperatures between 345 and 1000 K. After plasma exposure,

[6] D. Dasgupta, D. Maroudas, and B.D. Wirth, "Prediction of Temperature Range for the Onset of Fuzz Formation in Helium-Plasma-Implanted Tungsten," *Surface Science Letters* **698** (2020) 121614.

elemental composition as a function of sample depth was measured, as was surface morphology and nanofeatures in the film/substrate. At ≤750 K, no transport of Mo from the substrate into the W film is observed, and there is no indication of fuzz. At 800 K, Mo migration through the W film and pinholes (early phase of fuzz formation) are observed for the He-exposed sample. A lack of Mo migration and pinholes at an unexposed region of the sample and for a D-exposed sample suggests that material transport and morphology is He induced and not due to thermal processes. At 1000 K, a larger extent of Mo migration and fuzz development occurs.

In a second experiment, thin films of Mo of varying thickness (42-136 nm) were deposited on W substrates, exposed to a He plasma at a range of sample temperatures (840-1070 K) and analyzed. Fuzz formation and material mixing occurred for all samples. At each exposure temperature, the percentage of W at the surface is lower for samples with thicker Mo films since fuzz must grow beyond a certain thickness such that the bubble layer reaches the Mo-W interface. As expected from the first experiment, material transport and fuzz thickness increase with sample temperature for thin Mo films. Likewise, an increase in the concentration of W at the fuzz surface where fuzz forms is observed for the 64 nm sample exposed at 1070 K, illustrating that material transport outwards from the bulk during fuzz formation is independent of the choice of film and substrate materials. These measurements will be used to compare to various theoretical predictions for mechanisms of fuzz formation models, as well as scale bridging multiscale models.

Task 2. Integrating boundary plasma and PFC Surface models to predict PFC Performance
In order to integrate a comprehensive PMI coupling framework, both fluid and kinetic plasma models are being utilized and coupled to high-fidelity divertor models and SOL turbulence models. Our initial coupled models have focused on one-way coupling appropriate for investigating steady-state plasma operations, as was done in the FY2018 DOE Fusion Theory milestone. We have continued to extend and verify those simulation results, while also preparing to extend those simulations to evaluate the influence of mixed material formation on the plasma surface interactions, extending our efforts at experimental validation on both the DIII-D and WEST tokamaks, and performing analysis regarding the stability of the detached divertor conditions of importance to ITER.

Summary of Accomplishments (May 2019-April 2020):

- Evaluated impact of strong neon seeding on peak heat flux of the ITER divertor;
- Refined and re-run the integrated PSI modeling of ITER tungsten divertor performance during burning plasma operation, with expanded evaluation of the impact of helium plasma exposure;
- Initiated integrated PSI modeling of WEST tokamak helium plasma campaign C4; and
- Improved predictive modeling capability of tungsten net erosion in the DIII-D divertor.

Enhancements to sheath and erosion simulation (UIUC): PIC-BCA Development. Following the development of the PIC-BCA, issues with the BCA implementation in F-TRIDYN began to surface. First, F-TRIDYN cannot be compiled into a dynamic library for in-memory coupling. Since the code is a mix of Fortran 90/FORTRAN 77 and lacks modern code organization principles such as separation of common code blocks into functions or subroutines, development of a dynamic library version of F-TRIDYN would be prohibitively error-prone and time-expensive. Second, an undocumented issue with F-TRIDYN limits the minimum number of incident ions to 100, resulting in significant overhead on the order of 100X when coupling to a particle code where every plasma ion hitting the wall must run its own BCA trajectory. Third, anomalies in the energy-angle distributions of reflected ions in F-TRIDYN were detected. At certain ion-target and energy-angle combinations, artifacts such as erroneous, constant-angle peaks were found in the 2D distributions, and at low energy and normal incidence, helium on tungsten and helium on nickel reflected energy distributions disagreed with other BCA codes such as MARLOWE

and ACAT and molecular dynamics results[7] [8]. Fourth, the scattering angle calculation of F-TRIDYN uses the MAGIC algorithm of Ziegler; this algorithm is a fast approximation to the screened-coulomb scattering problem. In the literature, it is stated that the MAGIC algorithm deviates from the full solution of the screened coulomb scattering problem by as little as 2%, and that the mean deviation is 2.1%[9]. However, the accumulation of errors from the MAGIC algorithm over the course of an ion trajectory consisting of hundreds or thousands of ion-atom collisions results in significant deviations in quantities such as ranges, sputtering yields, reflection coefficients, and the energy-angle distributions of emitted particles. Fifth, F-TRIDYN's electronic stopping models, Lindhard-Scharff and Oen-Robinson, are limited to low energies (<25 keV/amu) and do not include experimentally observed Z1 oscillations in electronic stopping at low energy. Finally, the fractal surface routine in F-TRIDYN is not extendable to large-scale geometry, such as castellated tiles in a fusion device, due to the 1D planar surface binding energy model. This surface binding energy model limits F-TRIDYN's surface model to atomic-scale roughness. In light of these shortcomings of F-TRIDYN, the prototype of a new BCA has been developed in Python first (PyBCA), and then the development of a full, production-level BCA has been started in Rust (RustBCA). PyBCA, based on the best components of TRIM, SD.TRIM.SP, GEANT4, and original re-workings of critical BCA components, such as the surface binding energy and surface refraction model, served as a testbed for developing the new BCA. A production-level new BCA, intended to be more flexible than contemporary BCA codes and to be easy-to-use and develop in the hopes of supplanting the flawed SRIM[10] [11], has begun development in Rust. Rust is a modern, low-level, compiled language developed by Mozilla. Its primary feature is the replacement of a garbage collector or C-style memory management with a system known as the borrow-checker, which guarantees complete memory safety and effortless concurrency, a crucial advantage allowing for the fast development of new scientific codes. The newly developed BCA, RustBCA, already includes fixes for or planned features addressing each of the shortcomings outlined previously. It can be compiled as a dynamic library for in-memory coupling to the full C version of hPIC, it reproduces low-energy light ion reflection energy distributions from molecular dynamics and other BCA codes correctly, it includes a 6^{th}-order Lobatto quadrature to replace the MAGIC algorithm while retaining the MAGIC algorithm for comparison, it includes high-energy features such as Biersack-Varelas electronic stopping and the high-energy free flight path model from SRIM, and it has a full 2D geometry implementation allowing for the simulation of atomic- to macroscopic scale structures. RustBCA will be coupled to hPIC to produce a fast PIC-BCA, enabling the direct, fully-kinetic simulation of phenomena heretofore unapproachable with contemporary codes, such as dynamic redeposition in the divertor of a fusion device.

Improved hPIC Mesh. The previous uniform mesh of the hPIC code has been updated to a new implicit non-uniform mesh developed separately by RPI. Uniform meshes are inefficient in capturing the high plasma gradients in the magnetic and electrostatic sheaths forming in front of the material surfaces. In uniform meshes, the element size of the mesh for the whole domain is limited by the requirement of the smaller element size in the high-gradient sheath region. This requirement forces to over-sample the plasma bulk region where gradients are milder. To overcome all those issues, the hPIC Particle-In-Cell code has been modified to incorporate an implicit non-uniform mesh developed by the RPI team, to efficiently resolve large gradients in the plasma sheath region and not oversampling the plasma bulk region. The new mesh allows local refinement at the plasma sheath using a Boundary-Layer type of mesh, similar to meshes used in computational fluid dynamics. In implementing the new mesh, the UIUC team had to modify the stencil of the Poisson-solver using a generalized stencil function of the local grading ratio; modify the weighting function of the particles, modify the particle loading to account for the new

[7] V. Borovikov et al., *Journal of Nuclear Materials* **447** (2014) 254-270 (2014).
[8] Z. Luo et al., *Journal of Applied Physics* **75** (1994) 3789-3797.
[9] J. F. Ziegler et al., SRIM textbook (2008) Available on: http://srim.org/SRIM Book.htm
[10] V. Shulga, *Journal of Surface Investigation* **13** (2019) 562-565.
[11] K. Wittmaarck, *Journal of Applied Physics* **96** (2004) 2632-2637.

mesh. Thanks to the new mesh, the code now can handle large portions of plasma (e.g. linear plasma devices), still accurately resolving for the plasma sheath in front of the surface. The relaxed constraints on the mesh allow to reduce the simulation time by a factor of 10 to 100 times, depending on the problem, which opens a new paradigm of plasma problems to work with using hPIC. The current 1D multi-block implementation is currently being extended to a 2D multi-block case.

Applications of PSI models to ITER (ORNL,UTK): The SOLPS-ITER code has been used to explore mechanisms for reducing the peak fluxes and operating at a higher degree of detachment in ITER. For a fixed plasma shape, the peak heat flux can be reduced by increasing the divertor neutral pressure or by increasing the impurity concentration, actuated by deuterium and neon puffs, respectively. The existing simulation database[12] [13] was extended in these two directions using burning plasma conditions (Q_{DT} = 10, P_{SOL} = 100MW) in a standard shape (IMAS number 123013). Figure 14 shows the peak heat flux from the database (colored shapes connected with dashed lines) as a function of divertor neutral pressure for several values of the neon concentration evaluated as an average around the separatrix. The new cases are shown as star symbols, showing the peak heat flux can be reduced from 5 to 3 MW m^{-2} by increasing the divertor neutral pressure from 11 to 27 Pa by scaling the D and Ne puffs in equal amounts to keep the concentration approximately fixed at 0.2%. By increasing the Ne puff only, the heat flux can be significantly reduced to ~ 0.5 MW m^{-2}. As the concentration increases along this path, the position of the impurity radiation moves from the outer divertor towards the X-point under steady-state conditions. When the radiation front reaches the X-point, the core radiation becomes too large and steady-state solutions cannot be found. Ongoing work is exploring the compatibility of the steady-state solutions with core performance and using the database of SOLPS-ITER simulations to calculate momentum loss and cooling factors that go into a reduced model of detachment[14]. This reduced model can be used to develop simplified models for predicting divertor conditions in existing and future experiments.

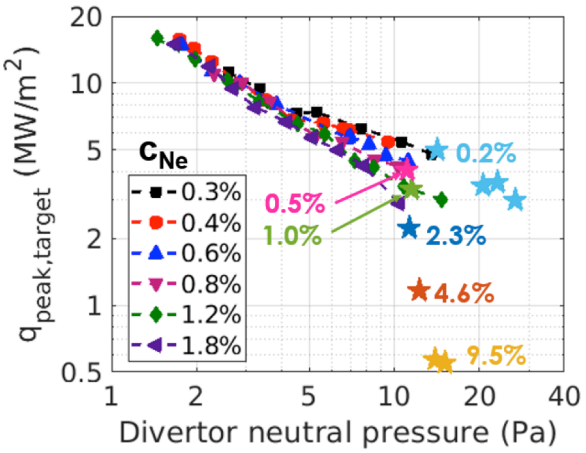

Figure 14. Peak heat flux at the outer divertor as a function of divertor neutral pressure for several values of neon impurity concentration from the SOLPS ITER database. Symbols indicate new simulations which extend the database performed as part of this work.

During the last year, integrated GITR-F-TRIDYN - Xolotl simulations of PISCES linear device experiments and ITER were completed, for both He plasma exposure and burning plasma operation (BPO). A manuscript that reports on the PISCES experiments and simulations is under preparation, nearing its final version. We have already published some of the findings from the ITER simulations, mainly focusing on He operations, and a more complete manuscript that includes the BPO scenarios is nearly ready for submission. However, recently we found some inconsistencies in the handling of SOLPS outputs of the ITER simulations, which will be described below, and are in the process of re-running the integrated model prior to publication. To further benefit from these re-runs, we will also look for the differences in the input to the surface model and explore the sensitivity of the surface response to these

[12] H.D. Pacher, et al., *J. Nucl. Mater.* **463** (2015) 591.
[13] R.A. Pitts, et al., *Nucl. Mater. Energy* **20** (2019) 100696.
[14] P.C. Stangeby, *Plasma Phys. Control. Fusion* **60** (2018) 044022.

changes coming from the SOL. While we expect the largest variations to be in the W flux to the surface, we anticipate that the over-all message regarding the surface response will remain the same.

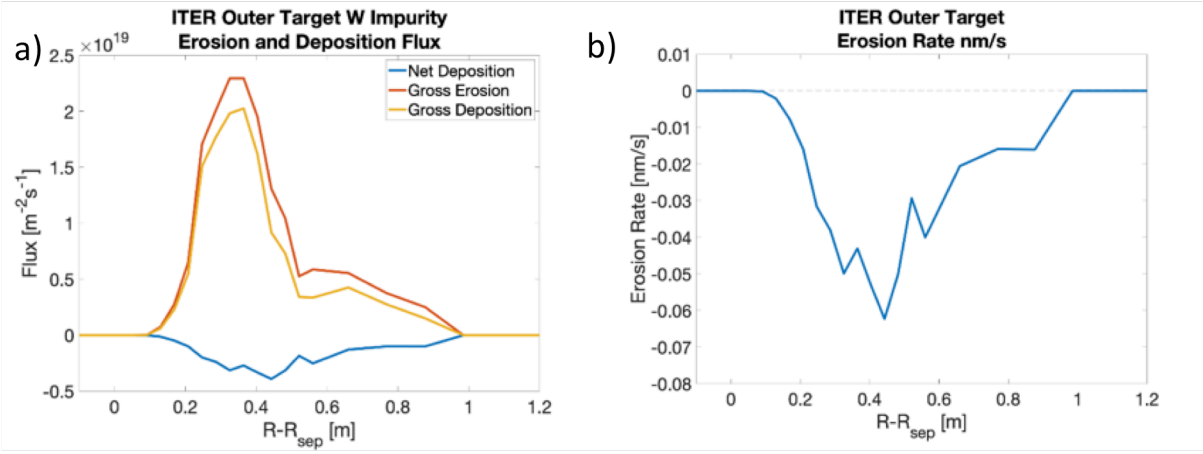

Figure 15. Updated profiles of a) tungsten erosion and deposition flux and b) net tungsten erosion rate predicted by GITR for the ITER 100 MW burning plasma operation.

During the continued processing and analysis of the integrated modeling of the plasma-surface interaction for ITER He and DT scenarios, an error was found in the processing of GITR output, which affected W flux and net erosion values. Steps have been taken to correct this, the integrated simulation components have been re-worked to verify known mistakes are fixed, and other processing scripts have been scrutinized to verify the accuracy. Work has also been performed to harden components, to enable automated testing and improved modularity. Processing of SOLPS output (geometry and plasma profiles) has been updated to ensure matching of SOLPS geometry and grid, accurate interpolation at the material boundary, gradients of potential and plasma temperature are accurately taken, and plasma flow velocity convention is correct. Plasma flow and gradients have a significant impact on the global migration of eroded W impurities, and near-surface interpolation affects the prompt re-deposition fraction of W in GITR. The integration of F-TRIDYN and hPIC results has been investigated to rule out potential numerical issues involving interpolation of results onto different grids. GITR results for gross and net erosion for ITER He operation have been updated, resulting in an increase in gross and net erosion increase of approximately a factor of 12.8 compared to the previously reported value. The gross deposition, erosion, and net erosion are shown in Figure 15, in which Fig. 15a) shows these values in the units of flux and Fig. 15b) shows the W erosion rate at the outer divertor target in nm/s. The propagation of this error into later aspects of the integrated simulation is still under investigation, as well as the effect on the simulations of ITER BPO.

Application of PSI models to WEST (ORNL): Predictive simulations were performed using SOLPS-ITER for helium plasma experiments performed in 2019 on WEST. The goal of these simulations was to estimate the expected fluxes at the probe used for material exposure, and to provide a background plasma solution for use in subsequent simulations. Using WEST shot 53034, which had deuterium as a main ion, experimental profile data at the midplane and the outer divertor were used to constrain the SOLPS simulations. Using the upstream profiles to determine appropriate cross-field transport coefficients, a fixed impurity concentration of a carbon-like radiator was scaled until the divertor probe data was approximately matched. Figure 16 shows an example, with the parallel current density profile from the probe (black dots) and from SOLPS for several levels of impurity concentration (colored lines). A best is fit is found for a concentration of 3.65%.

Using the transport coefficients and impurity concentration levels from the deuterium simulations, the case was repeated for helium as the main ion. The background plasma solution was then made available to the SciDAC team for subsequent simulations, including divertor data formatted for input into hPIC and Fractal TRIDYN. The same interpretive procedure described above is also in progress using the experimental data obtained from the 2019 experiments.

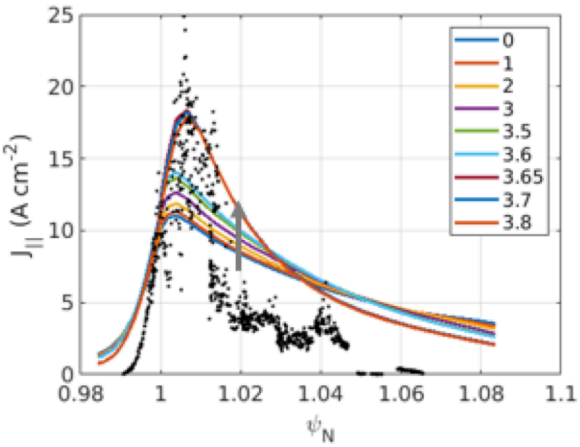

Figure 16. Profile of parallel current density at the outer divertor from probes (black dots) and SOLPS (colored lines as a function of impurity content). A best fit is found for an impurity concentration of 3.65%.

Progress toward predictive modeling and in-situ monitoring of tungsten net erosion in the DIII-D divertor (GA): Fundamental mechanisms governing the prompt re-deposition of tungsten impurities sputtered in tokamak divertors have been identified and analyzed to enable quantitative estimations and in-situ monitoring of the net erosion and lifetime of tungsten divertor plasma-facing components in ITER and future fusion reactors. The net erosion of tungsten divertor PFCs is primarily determined by the prompt re-deposition of tungsten impurities, which is very large in the high-density partially attached divertor plasma conditions expected for instance in ITER operational divertor scenarios. Near the divertor targets, the width of the electric sheath is of the order of several main ion Larmor radii due to the magnetic field lines intersecting the material surfaces at grazing incidence, and a vast majority of tungsten impurities sputtered from divertor PFCs are thus ionized multiple times within the sheath region[15].

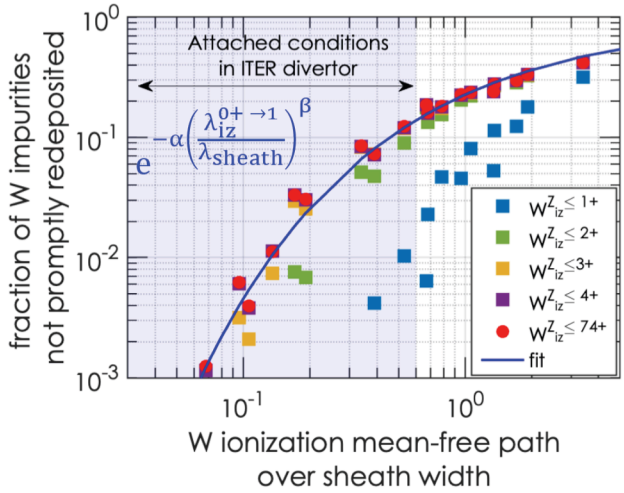

Figure 17. Fraction of W impurities not promptly redeposited as a function of the vertical ionization mean-free path of neutral tungsten over the sheath width.

The complex interplay between the successive ionizations of tungsten impurities sputtered from divertor PFCs and the sheath electric field is shown to ultimately govern the prompt re-deposition of tungsten in the divertor region, as illustrated in Figure 17. Consequently, the fraction of sputtered tungsten impurities that do not promptly re-deposit, and therefore contribute to the net erosion of tungsten PFCs mainly depends on the ratio of the vertical ionization mean-free path of tungsten neutrals over the sheath width. A new scaling law quantifying the prompt re-deposition of high-Z impurities in divertor has been derived[16], and is shown as the blue curve in Fig. 17. This new scaling law significantly differs from the scaling law

[15] J. Guterl, et al. *Analysis and model validation of tungsten prompt redeposition in tokamak divertor* 61st Annual Meeting of the APS Division of Plasma Physics Fort Lauderlale, FL, USA (2019).
[16] J. Guterl, et al. *On the erosion and re-deposition of tungsten in tokamak divertor* 17th International Workshop on Plasma Edge Theory in Fusion Devices, La Jolla, CA, USA (2019).

conventionally used for low-Z impurities, since effects of the sheath electric field are much stronger on trajectories of high-Z impurities than on trajectories of low-Z impurities, due to the larger mass of high-Z impurities. Tungsten prompt re-deposition is predominantly governed by the tungsten ionization rates and the width of the sheath within this new scaling law. As well, S/XB coefficients (number of ionization events per photon) for high-Z impurities like tungsten are significantly reduced in high-density divertor plasma conditions when sputtered impurities are ionized within the sheath region, where electrons are repelled by the sheath electric field. This highlights that the modification of the electron distribution in the sheath region must be taken into account to accurately estimate the ionization and emission rates and derive the S/XB coefficients used to determine the flux of impurities from divertor PFCs.

Task 3. Dynamic wall response & feedback to divertor plasma

The goal of this thrust is to develop fundamental understanding of the temporal dynamics of the interaction between plasma and material surfaces at the edge of magnetically confined fusion energy devices. Do these interactions cause new types of coupled plasma-wall oscillations and instabilities? Will plasma-wall interactions change the character of turbulence near material surfaces? The objectives of the research program, co-led by Ilon Joseph (LLNL) and Sergei Krashenninikov (UCSD), are to develop predictive computational models of plasma-material interactions (PMI) for two of the most important outstanding issues:

1. Material surface erosion due to transient power and particle loads, and,
2. Dynamic recycling of main ions and impurity species between the plasma and wall.

In order to develop predictive capability, high-fidelity models for both the edge plasma and material PFCs must be coupled together. The goal is to perform the first studies of dynamic recycling and material erosion caused by transient events that include kinetic effects from the SOL plasma to the sheath to the material surface.

During this reporting period, we extended our studies of impact of dynamic wall outgassing on edge plasmas of fusion devices to modeling of a sequence of multiple ELM-like plasma heat pulses.

Summary of Accomplishments (May 2019-April 2020):

• Implemented logical sheath BCs within the COGENT code and explored physics of ELM heat-pulse model with kinetic electrons;
• Implemented neutral ionization particle sources and charge-exchange friction forces within BOUT++ divertor turbulence model;
• Completed linear and nonlinear divertor turbulence verification studies without neutrals in straight magnetic field geometry;
• Initiated linear and nonlinear divertor turbulence verification studies with neutrals and compared to analytic theory;
• Coupled UEDGE plasma code to FACE wall code and explored dynamic recycling of steady-state, single ELM pulses and multiple ELM pulses; and
• Discovered that an ELM can induce detachment by heating PFCs that are saturated with neutrals and releasing this neutral gas into the plasma.

Dynamic recycling during ELMs and transient events (LLNL, UCSD, GA): A coupled plasma-wall model exchanges heat and particle fluxes between the UEDGE plasma transport code and the FACE advection-diffusion code, which tracks the transport and trapping of hydrogenic species within material walls. Due to the fact that both codes utilize nonlinear solvers for implicit time integration and offer great flexibility in specifying the physics of the models, this tool is very fast and should be ideal for phenomenological studies of experimental data. With this tool, we can also explore coupling algorithms, verify the more complete coupled models, and explore the physics of dynamic recycling during ELMs and under detached plasma conditions.

Figure 18 illustrates the predictions of the coupled UEDGE-FACE workflow during a single ELM event. In this higher density case, the ELM induces divertor plasma transition to detachment because it releases significant amounts of hydrogen trapped in the wall. Further investigations of this model have extended the simulation to over 30 ELM cycles, corresponding to one second of simulated time. We have developed a plan for extending this model to 2D UEDGE simulations and for a series of 1D FACE simulations along the wall that can be performed in parallel. We believe that this process will be streamlined and better integrated with the Integrate Plasma Simulation (IPS) coupling framework by switching to the python version of UEDGE (pyUEDGE).

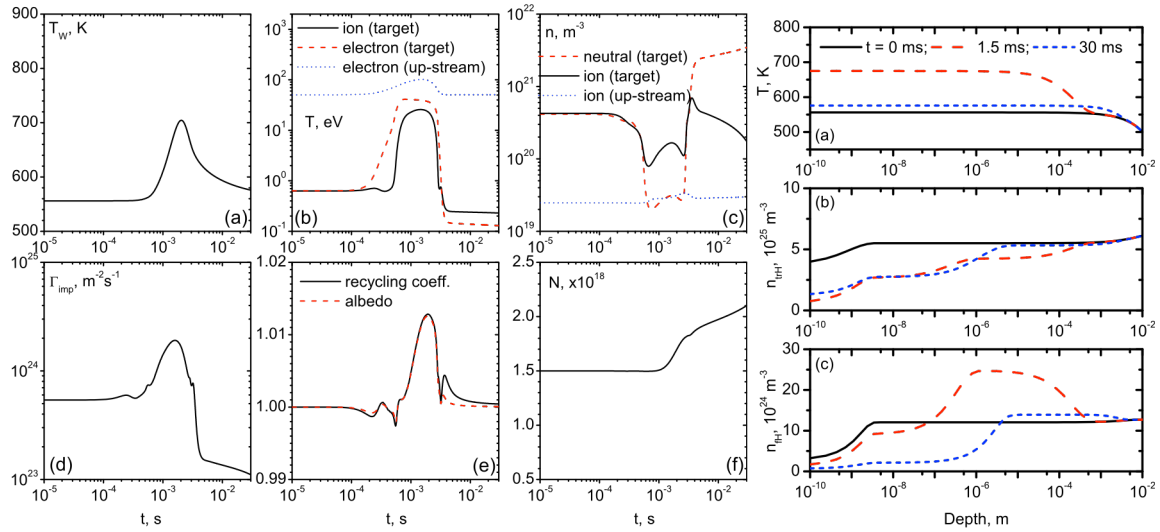

Figure 18. Dynamic recycling simulated by the coupled UEDGE-FACE workflow for an ELM-like transient pulse of particles and heat. Left panel: (a) wall surface temperature, T_w, (b) ion and electron temperatures, T, (c) ion and neutral densities, n, (d) particle flux, Γ_{imp}, (e) recycling and albedo coefficients, (f) total particle number, N, versus time, t. Right panel: (top) wall temperature T, (middle) free hydrogen density, and (bottom) trapped hydrogen density for three different times, t = 0, 1.5, and 30 ms.

In continuation of our studies of the dynamic coupling of edge plasma and hydrogen retention/outgassing from divertor target plate, we investigated the long-term evolution of the coupled plasma-wall system during series of multiple ELM-like heat pulses. The simulations were performed in one-dimensional geometry representing a narrow magnetic flux surface in the SOL region. The simulated system comprised of deuterium plasma, including nitrogen impurities with a non-uniform density profile in divertor region, and the divertor target of 1 cm thickness. The target material parameters were chosen corresponding to tungsten and included hydrogen traps with de-trapping energy of 0.9 eV, uniformly distributed with density of 0.1 at.% in the material. The coupled FACE-UEDGE codes solve plasma transport equations including atomic physics and the hydrogen reaction-diffusion together with the heat conduction equations in the wall. The total number of particles in the system was conserved. The plasma heat source was uniformly distributed in the upstream SOL region above the X-point. The particle and energy fluxes at the plasma-material interface were exchanged between the codes, providing dynamic hydrogen recycling and wall heating. The wall temperature at the side not exposed to plasma was kept constant at 500 K. The initial system state corresponded to a steady state determined by a given total hydrogen content of the plasma. The ELM-like heat pulses were simulated by varying in time the plasma heating power. The pulses had $\sim\sin^2(\pi t/\tau)$ temporal profile with the duration τ=3 ms and the magnitude corresponding to 15 times of the steady-state heating power. The pulses repeated every 30 ms for total of approximately 1 s of simulated evolution.

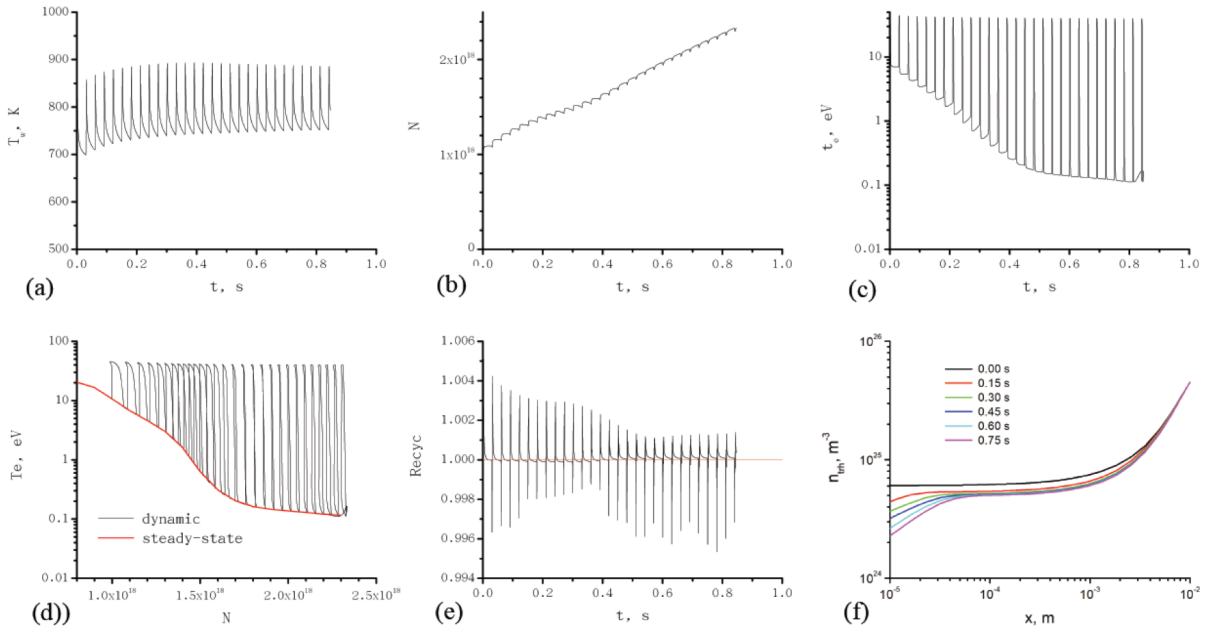

Figure 19. (a) The simulated temporal evolution of the wall surface temperature; (b) the total number of plasma hydrogen particles; (c) the electron temperature near the wall; (d) evolution of the plasma electron temperature near the wall as function of the number of plasma particles; (e) the recycling coefficient, and (f) the trapped hydrogen profile in the wall.

The simulation results illustrated in Figure 19 demonstrate that the sequence of the heat pulses leads to gradual increase and eventual saturation of the average wall surface temperature, while each pulse produces a sharp temperature spike. The wall temperature dynamics causes gradual increase of the total number of particles in the plasma, as the hydrogen is released from the material. This induces large drop of the inter-pulse plasma temperature near the wall representing transition to divertor detachment. We note that in this case the detachment is induced over tens of the heat pulses. In more extreme cases, divertor detachment can be induces even by a single pulse, as was shown in our previous work, which depends on the initial plasma state, the hydrogen profile retained in the wall, and the magnitude of the heat pulse. It is also important to note that the electron temperature sharply increases to the same peak value during each heat pulse, causing transient plasma re-attachment independent on the pre-pulse plasma conditions. We found that the inter-ELM plasma conditions are very close to a steady state corresponding to a current plasma hydrogen content, Fig. 19d. This is due to the short plasma response time to wall outgassing, which is of order of a few milliseconds. The simulations show that the plasma recycling on the divertor target is evolving over number of pulses, Fig. 19e. In the first ~0.4 s, the hydrogen is net released during the pulses and then is slowly reabsorbed by the wall in the inter-pulse periods. However, at the later stages, as the material surface layer becomes depleted, Fig. 19f, the hydrogen is net absorbed during the ELM-like pulses and is slowly released from deeper in the material during the inter-pulse periods. The simulated recycling dynamics demonstrates complex response of the wall outgassing to plasma perturbations, which depends on the hydrogen profiles in the material with the longer response times corresponding to the deeper material layers. Such dynamics gives rise to memory effects when the wall response depends on the history of the material's plasma exposure. The results demonstrate key physical mechanisms by which plasma-wall coupling can affect divertor plasma conditions, and which are important for understanding of role of the dynamic wall retention in various edge plasma phenomena.

A quasi-linear analysis of the dynamic outgassing response of tungsten plasma facing components to fluctuations of plasma particle and heat fluxes has been performed using the reaction-diffusion model

embedded in FACE. The characteristic frequency $\boldsymbol{\omega_{cutoff}}$ of the wall response was obtained as the superposition of the outgassing responses from the material surface and from the material bulk as function of hydrogen transport, trapping and desorption from tungsten material. It is shown that the outgassing response from tungsten bulk is determined by the diffusive transport of hydrogen in bulk, whereas the outgassing response from tungsten surface is determined by the molecular recombination of hydrogen.

The dynamic outgassing response of tungsten wall is controlled by surface processes when tungsten surface is not saturated with hydrogen (Figure 20). However, the saturation of tungsten material surface with hydrogen may significantly accelerate the surface response, and the outgassing response to plasma fluctuations from tungsten wall material becomes virtually instantaneous (Figure 20).

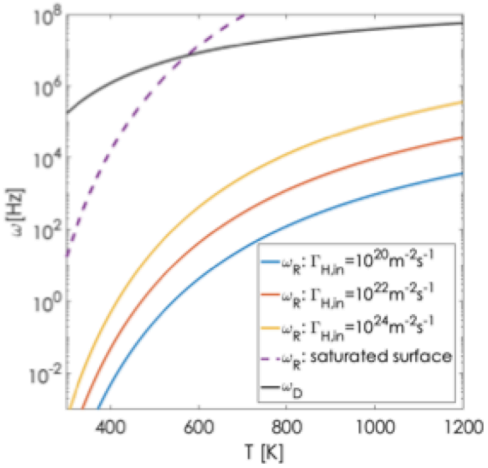

Figure 20. Characteristic frequency of tungsten bulk (ω_D) and surface outgassing response (ω_R) to plasma fluctuations as a function of temperature.

Molecular dynamics simulations have been conducted with LAMMPS to estimate the activation energies and cross-sections characterizing hydrogen recombination and desorption from tungsten surfaces using the most recent EAM W-H interatomic potential. The activation energy and cross section for hydrogen thermal molecular desorption from tungsten surface calculated with molecular dynamics simulations are shown to be comparable to experimental measurements at low hydrogen surface concentration. At high hydrogen surface coverage, a large decrease of the activation energy of hydrogen recombination from 1.4 eV to 0.8 eV is observed, in agreement with experimental observations of fast desorption of hydrogen from saturated tungsten surface.

Furthermore, cross-sections of ion-induced desorption process were estimated from the bombardment of tungsten surface at a coverage of 1:2 in MD simulations as a function of the energy of the impinging H particles. It is shown that the Eley-Rideal desorption process becomes significant at low energy ($E_0 < 10eV$) while ion-induced atomic desorption becomes significant at higher energy ($10eV < E_0 < 100eV$). Recent experimental observations in DIII-D suggest that such ion-induced desorption from tungsten take place during ELMs[17].

Dynamic recycling turbulence model (LLNL, UCSD): A new divertor-relevant turbulence model, called SOLT3D, has been implemented within the BOUT++ framework. The physics model is based on the 2D SOLT divertor turbulence model developed by Jim Myra (Lodestar), who is also a collaborator on the development of SOLT3D. The physics model has recently been upgraded to include the neutral density n_n, in addition to the ion density n_i, the electron temperature T_e, the electric potential ϕ, and the parallel vorticity ϖ (fluid version of the gyro-Poisson equation) in a simplified mapped geometry appropriate for the divertor leg. With this equation set, the model includes the physics of the most relevant modes of instability: resistive ballooning modes and drift waves. The model also includes a linearized version of sheath BCs, which induce the "conducting wall mode," one of the most important modes to consider for turbulence near the divertor target plates. We have performed linear verification tests of these modes of instability and have successfully checked the new results against analytic theory and past simulation models. We have also performed nonlinear verification tests for plasma turbulence in straight magnetic field geometry modeled on the LArge Plasma Device (LAPD).

[17] I. Bykov, et al. *Physica Scripta* **T171** (2020) 014058.

The impact of neutral-plasma interactions on divertor turbulence is now a major focus of activity. A recent investigation of the impact of neutrals on the linear growth rate of the drift-resistive ballooning mode, shown in Figure 21, demonstrates that the growth rate is enhanced by increased ionization and reduced by neutral-ion friction, as predicted by analytic theory. A strategy for coupling to the wall codes, FACE and Xolotl (which predict neutral outflux), is under development. The coupled code will become our primary tool for studying the interplay between dynamic recycling processes and divertor turbulence.

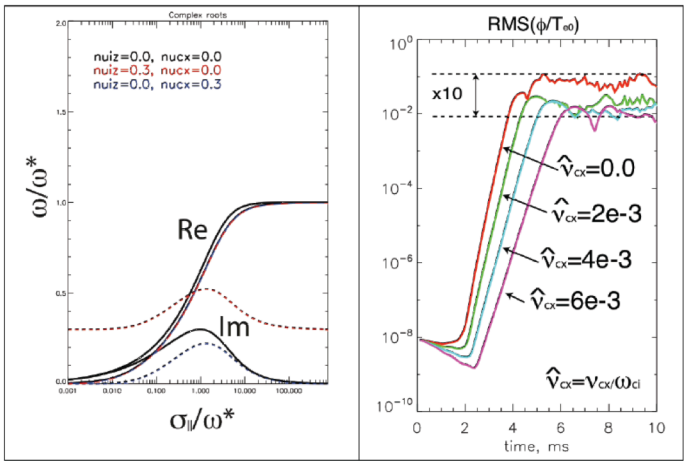

Figure 21. SOLT3D predictions of the impact of neutral-plasma coupling on divertor turbulence. Left: the growth rates of drift-resistive ballooning modes (black solid) are increased by adding ionization (red dashed) and reduced by adding charge exchange (blue dashed). Right: the turbulence amplitude during both the linear growth phase and the saturated steady-state are reduced by increasing the charge exchange frequency, ν_{cx}, due to neutral ion friction.

Kinetic simulation of an ELM pulse (LLNL): We implemented an ELM heat pulse model within the guiding center COGENT code. The model uses kinetic guiding center ions, and, for electrons, it can either use a Boltzmann model or kinetic guiding center model with logical sheath BCs. We are still in the process of verifying the kinetic electron model by studying the well-known ELM benchmark problem: simulating an ELM heat pulse under conditions relevant to the Joint European Torus (JET) tokamak pedestal and SOL. The COGENT prediction for the initial burst of electron heat flux using the 1D+2V kinetic ion and kinetic electron model is shown in Figure 22. These 1D+2V results, using the actual electron mass, are in qualitative agreement with previous studies; however, we are investigating whether switching to a different version of the logical sheath BCs would improve agreement.

The parameters of the model (T_{ped} = 1.5 keV, n_{ped} = 10^{19} m^{-3}) place the simulation in the collisionless regime, and the outflowing electron distribution is strongly non-Maxwellian. The electron transit time is only ~2 ms, so, by the time of the peak of the initial electron heat burst at t = 6 ms, the electrons have already developed a large fraction of trapped particles, as shown in Figure 23a. As was found previously for the ion distribution, the Maxwellian source of particles and heat at the midplane causes the electron distribution at the midplane to become asymmetric in parallel and perpendicular energy. The asymmetric electron distribution at the midplane shown in Figure 23b can be explained as being due to the balance between parallel advection and the Maxwellian source and leads to a distribution that approaches a Maxwellian divided by $|v_{||}|$ at large $v_{||}$. The distribution also prominently displays two different populations corresponding the hot

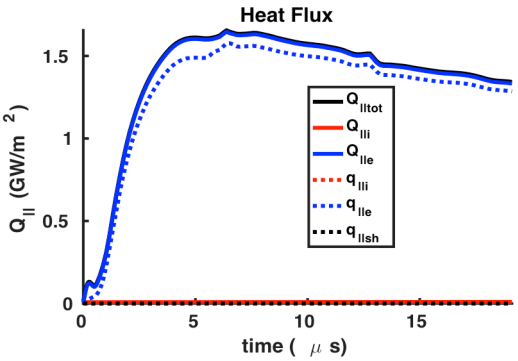

Figure 22. COGENT prediction for the initial electron heat flux burst generated by a 0.4 MJ edge-localized mode (ELM) for a benchmark case corresponding to parameters for the Joint European Torus (JET) tokamak. Collisionless simulation results with kinetic ions and, now, with kinetic electrons: total heat flux $Q_{||,tot}$ (blue), total ion heat flux $Q_{i,||}$ (solid red), ion heat flux incident on sheath $q_{i,||}$ (dotted red), additional ion sheath heat flux $q_{i,sh}$ (dotted black), electron heat flux $Q_{e,||}$ (solid black).

ELM injection energy, 1.5 keV, and the cold initial electron temperature, 75 eV.

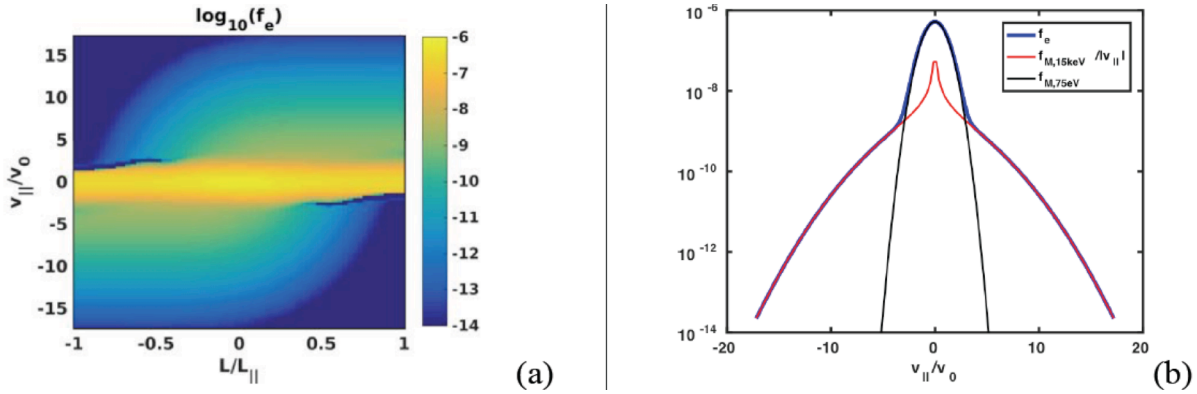

Figure 23. The collisionless electron probability distribution function (PDF) predicted by COGENT for the benchmark 0.4 MW edge-localized mode (ELM) case corresponding to Joint European Torus (JET) tokamak parameters at t = 6 ms after the ELM is initiated. **(a)** The PDF as a function of normalized parallel velocity and length shows the formation of an electron population trapped by the sheath potential. **(b)** Comparison of the electron PDF at the midplane for a collisionless simulation (blue) to a Maxwellian distribution corresponding to the cold 75 eV initial temperature (black) and a Maxwellian / $|v_{||}|$ corresponding to the hot 1.5 keV pedestal source (red).

These kinetic electron and ion simulations are quite challenging to push to ion timescales because they use explicit time integration and the time step is set by the CFL condition associated with the extremely fast electrostatic Alfven wave (ESAW). For these simulations, we have used the approach of Shi, Hakim, and Hammett[18] in controlling the ESAW velocity by constraining the electric potential to be proportional to the charge density. This approach allows one to set the ESAW speed to be somewhat larger than the electron thermal speed. However, when using this method, the CFL condition is set by the speed of the fastest electrons, which still makes the time step ~60 times smaller than in the Boltzmann electron case.

Milo Dorr and Debojyoti Ghosh at LLNL's Center for Applied Scientific Computing (CASC) have implemented implicit time-stepping capabilities for the electron advection operator using additive Runge-Kutta (ARK) time integrator framework in COGENT. As described in the CS/AM section, they have successfully applied these capabilities to a number of test problems and have already demonstrated the ability to take time steps 100x larger than the CFL limit for the ELM heat pulse model with Boltzmann electrons. We expect that this work will soon lead to great improvements in computational efficiency for coupled kinetic electron-kinetic ion problems.

FUTURE PLANS

Computer Science/Applied Math activities:

Plans for next year are to continue to well integrate the computer science and applied mathematics activities into the 3 research tasks, continuing our focus of extending hPIC and GITR for non-structured meshes, engaging in dynamic code coupling utilizing the IPS framework, and to continue the implementation of a GPU version of Xolotl. On the UQ front, we will combine what has been learned about Xolotl and F-TRIDYN into a coupled analysis using the IPS framework. This will involve running the coupled F-TRIDYN-Xolotl simulations to build PC surrogates for GSA, while using sparse quadrature methods and in-situ adaptive sparse quadrature methods (using the DAKOTA software), to ameliorate the cost of the coupled setting. This will lay the groundwork for subsequent efforts where the

[18] Shi, Hakim, and Hammett, *Phys. Plasmas* **22** (2015) 022504.

coupling will be expanded to GITR and other codes in the IPS workflow, where the lessons learned in the F-TRIDYN-Xolotl case will be used to scale up capabilities more rapidly and efficiently for the UQ investigation.

TASK 1. PFC Surface Response (Scale-bridging to extend capability of Xolotl PFC Simulator) activities:
On the SNAP potential development front, we are currently extending the W-Be potential to include hydrogen. Similar to our treatment of nitrogen, we fit a potential for pure hydrogen in order to reproduce the expected dimer and trimer binding curves as well as the dynamic behavior of hydrogen gas. SNAP successfully reproduces both binding curves, better reproduces the DFT energies compared to an existing W-H EAM potential developed by Wang *et al.*[19] and prevents the formation of larger clusters in dynamical simulations of H_2 molecules at 1000 K, similar to SNAP nitrogen. The potential will be extended to W-H and fitted to reproduce material properties such as the hydrogen defect formation energies and adsorption energies in tungsten. Beryllium will then be added back into the fitting and a full W-H-Be potential will be developed.

The large-scale MD simulations will focus on establishing an atomistic database of the sub-surface gas dynamics of helium bubbles and hydrogen isotopes for conditions of mixed beryllium – tungsten surface evolution, which will be used to benchmark the parameterization of Xolotl for simulating plasma surface interactions of mixed materials. Future research on developing a database for thermomechanical properties of PFC tungsten focuses on: (a) atomic-scale computation of *mechanical properties beyond the elastic regime*, including strength, toughness, ductility, and analysis of fracture mechanics and embrittlement effects; (b) atomic-scale computation of *thermal expansion coefficients* and their dependence on the thermomechanical state of PFC tungsten for development of continuum-scale models to compute thermal stresses in PFC tungsten; (c) computation of the *interfacial free energy per unit area* of the He/tungsten bubble/matrix interface for closure (i.e., development of constitutive models) of continuum-scale models for the surface morphological response of PFC tungsten; and (d) atomic-scale computation of the *thermal conductivity* of PFC tungsten (as a function of thermomechanical state and defect size/bubble pressure) for incorporation into heat transfer models for determining the temperature distribution in PFC tungsten.

The focus of the scale-bridging continuum scale simulations involves predicting plasma surface interactions, involving both surface topology changes and net erosion, as well as the hydrogen isotope recycling, retention and permeation for real-world conditions of fusion tokamak performance involving mixed materials. These efforts will include experimental validation through comparisons with measurements performed on the DIII-D and WEST tokamaks, as well as predicting the performance of the tungsten divertor during ITER operation within the integrated PSI modeling framework developed within Task 2 for steady state operation, and within Task 3 for transient plasma conditions.

TASK 2. Integrating boundary plasma and PFC surface models to predict PFC Performance
Near-term research will primarily focus on continuing the integrated simulations, including the re-runs of the ITER cases with the corrected values for tungsten erosion and re-deposition. New integrated simulations will also be performed in support of the WEST experiments exposing tungsten to helium plasmas. As described above, the background plasma simulations have been performed using SOLPS-ITER. Analysis of the sheath and erosion using F-TRIDYN under these conditions are underway, and will inform future simulations using the full GITR-FTRIDYN-Xolotl workflow. These experiments will provide an important opportunity to validate the simulations under conditions that are closer to idealized that is typically possible.

[19] L.-F. Wang et al., *J. Phys.: Condens Matter* **29** (2017) 435401.

A major future research area that we expect to carry through the rest of the project is enhancing the integrated simulations workflow to accommodate time-varying plasma conditions (associated with Task 3 activities). It is well-established that edge-localized modes (ELMs) are the dominant source of tungsten erosion, especially under detached divertor conditions where the ion impact energies are largely below the threshold for tungsten sputtering. In these cases the high-energy ions carried by ELMs dominate sputtering, and hence the erosion characteristics. These will be simulated by first producing SOLPS-ITER simulations that include a mock up of ELMs by introducing temporarily increased transport coefficients[20]. We aim to produce simulations that contain several ELMs, with multiple ELM sizes considered. These will then used to drive the GITR-FTRIDYN-Xolotl integrated workflow by providing a time-varying background plasma and incident particle and heat fluxes. Initial efforts will still focus on one-way coupling, without aiming to include the reaction of the plasma to the time-varying surface interactions. Such simulations will be considered in the future through coordinated research with Task 3. Task 3 is also performing ELM simulations based on kinetic plasma simulations, and when combined with the work to be carried out within Task 2 will allow a comparison to be made evaluating the impact of including kinetic plasma effects vs. relying on fluid modeling.

TASK 3. Dynamic wall response & feedback to divertor plasma

The focus of activities within the next year include utilizing the implicit time integration capabilities within COGENT for simulating the electron kinetics during an ELM, and to perform ELM heat pulse simulations for ITER-relevant strategies. We have recently implemented a user group between Task 2 and Task 3 researchers to evaluate the use of IPS as the code coupling framework for dynamic feedback amongst our PSI codes, and we will extend that activity to provide a more complete roadmap for the physics simulation and validation targets that involve coupling COGENT to hPIC and for multi-dimensional coupling of the background plasma models to F-TRIDYN and Xolotl, in addition to evaluating the verification and validation of linear and non-linear divertor turbulence studies.

MILESTONES for Years 4 & 5

The milestones specified in the original proposal for years 4 and 5 are reproduced below. The work underway in our project, which we have described within this report, is well aligned with these original milestones, and the future activities we have initiated will well position us to meet these milestones without the need for any modification at this time.

- Benchmarking Xolotl for mixed W-Be-He-H gas dynamics and surface evolution to large-scale MD & AMD simulations
- KMC/MD models of thermal-mechanical properties during transient plasma conditions (ELMs), up-scaled to Xolotl to predict cracking & dust formation of W surfaces and de-lamination of W-Be co-deposits
- Coupled boundary plasma-surface evolution simulations of ITER tungsten divertor tiles, including Be impurities deposition to evaluate fuel recycling and tritium retention
- Extend transient evolution workflow to include feedback on plasma; large-scale analysis of sheath turbulence and two-stream instabilities; investigate physics of plasma-wall coupling addressing the ELM cycle and detachment dynamics

[20] D.P. Coster, *Journal of Nuclear Materials* **390-391** (2009) 826-829.

Appendix 1: Project Bibliography

Peer-Reviewed, Archival Journal Publications:

2020:

- D. Dasgupta, D. Maroudas, and B. D. Wirth, Prediction of temperature range for the onset of fuzz formation in helium-plasma-implanted tungsten, Surface Science **698**: 121614 (2020).
- A Lasa , J M Canik, S Blondel, T R Younkin, D Curreli, J Drobny, P Roth, M Cianciosa , W Elwasif, D L Green and B D Wirth, Multi-physics modeling of the long-term evolution of helium plasma exposed surfaces, *Physica Scripta* **T171** (2020) 014041
- W. R. Elwasif ; A. Lasa ; P.C. Roth ; T. R. Younkin ; M. R. Cianciosa, Nested Workflows for Loosely Coupled HPC Simulations, *2019 IEEE/ACS 16th International Conference on Computer Systems and Applications (AICCSA)*, Abu Dhabi, UAE, 2019, pp. 1-8
- A. Weerasinghe, B. D. Wirth and D. Maroudas, Elastic properties of plasma-exposed tungsten predicted by molecular-dynamics simulations, ACS Applied Materials & Interfaces **12**: 22287−22297 (2020).
- L. Yang and B. D. Wirth, First-principles study of hydrogen behavior near W/WC interfaces, Journal of Applied Physics **127** (11): 115107 (2020).
- K. D. Hammond, D. Maroudas, and B. D. Wirth, Theoretical Model of Helium Bubble Growth and Density in Plasma-Facing Metals, Scientific Reports **10**: 2192 (2020).
- N. Mathew, D. Perez, E. Martinez, Atomistic simulations of helium, hydrogen, and self-interstitial diffusion inside dislocation cores in tungsten, Nuclear Fusion **60**: 026013 (2020).
- K. D. Hammond, Parallel Point Defect Identification in Molecular Dynamics Simulations Without Post-Processing: A Compute and Dump Style for LAMMPS, Computer Physics Communications **247**: 106862 (2020).
- R. D. Smirnov, S. I. Krasheninnikov, and M. V. Umansky, Time-dependent modeling of coupled plasma-wall dynamics, Physics of Plasmas **27** (3): 032503 (2020). (Editor's Pick)
- M. J. Baldwin, A. Založnik, R. D. Smirnov, and R. P. Doerner, Experimental measurements and modeling of the deuterium release from tungsten co-deposited layers, Nuclear Materials and Energy :100743 (2020, in press) doi: 10.1016/j.nme.2020.100743
- J. Guterl, T.Abrams, C. Johnson, A.E. Jaervinen, H. Q. Wang, A.G. McLean, D.L. Rudakov, W.R. Wampler, H. Guo, and P. B. Snyder, ERO modeling and analysis of tungsten erosion and migration from a toroidally symmetric source in DIII-D divertor, Nuclear Fusion **60** (1): 016018 (2020).
- O. El-Atwani, W. S. Cunningham, D. Perez, E. Martinez, J. R. Trelewicz, M. Li, S. A. Maloy, *Temperature threshold for preferential bubble formation on grain boundaries in tungsten under in situ helium irradiation*, Scripta Materialia, **180** (2020) 6-10.
- E. Martinez, M. J. Caturla and J. Marian, DFT-Parametrized Object Kinetic Monte Carlo Simulations of Radiation Damage, Handbook of Materials Modeling: Applications: Current and Emerging Materials, Springer, 2020.

2019:

- S. Keniley, D. Curreli, Density Estimation Techniques for Multiscale Coupling of Kinetic Models of the Plasma Material Interface, Journal of Computational Physics **400**: 108965 (2019).
- Diamond, G., Smith, C.W., Yoon, E., Perumpilly, G., Sahni, O. and Shephard, M. S., Towards Accelerated Unstructured Mesh Particle-in-Cell. In 2019 IEEE/ACM 10th Workshop on Latest Advances in Scalable Algorithms for Large-Scale Systems (ScalA), pp. 42-51, (2019).
- L Yang and B. D. Wirth, First-principles study of hydrogen diffusion and self-clustering below tungsten surfaces, Journal of Applied Physics **125** (16): 165105 (2019).
- D. Maroudas and B. D. Wirth, Atomic-scale modeling toward enabling models of surface nanostructure formation in plasma-facing materials, Current Opinion in Chemical Engineering **23**: 77–84 (2019).

- J. Guterl, R.D. Smirnov and P. Snyder, Effects of surface processes on hydrogen outgassing from metal in desorption experiments, Nuclear Fusion **59** (9): 096042 (2019).
- D. Dasgupta, R. D. Kolasinski, R. W. Friddle, L. Du, D. Maroudas, and B. D. Wirth, On the origin of "fuzz" formation in plasma-facing materials, Nuclear Fusion **59** (8): 086057 (2019).
- K. D. Hammond, I. V. Naeger, W. Widanagamaachchi, L.-T. Lo, D. Maroudas, and B. D. Wirth, Flux Effects on Helium Bubble Growth and Surface Morphology in Plasma-Facing Tungsten from Large-Scale Molecular Dynamics Simulations, Nuclear Fusion **59** (6): 066035 (2019).
- M.A. Wood, M.A.Cusentino, B.D. Wirth, and A. Thompson, "Data-driven material models for atomistic simulations", Physical Review B ***99*** (2019) 184305
- Z. J. Bergstrom, C. Li, G. D. Samolyuk, B. P. Uberuaga, and B. D. Wirth, Hydrogen interactions with low-index surface orientations of tungsten, Journal of Physics: Condensed Matter **31** (25): 255002 (2019).
- I. Joseph, M. A. Dorf, and M. R. Dorr, Simulation of Edge Localized Mode Heat Pulse Using Drift-Kinetic Ions and Boltzmann Electrons, Nuclear Materials and Energy **19**: 330–334 (2019).
- J. Guterl, W. R. Wampler, D. L. Rudakov, T. Abrams, H. Q.Wang, A. G.McLean, and P. B Snyder, Reduced model of high-Z impurity redeposition and erosion in tokamak divertor and its application to DIII-D experiments, Plasma Physics and Controlled Fusion **61** (12)**:** 125015 (2019).
- J. Guterl, C. Johnson, D. Ennis, S. Loch and P. B. Snyder, Effects of the Chodura sheath on tungsten ionization and emission in tokamak divertors, Contributions to Plasma Physics (2019).

Presentations:

2020 (January – April):

- E. Martinez, N. Mathew, D. Perez, D. Maroudas, B. Wirth, "Thermal gradient effect on the helium and intrinsic defects transport properties in Tungsten", APS March Meeting, March 2020.
- N. Mathew, E. Martinez, D. Perez, " Accelerated Molecular Dynamics Simulations of Dislocation-Obstacle Interactions in Tungsten: Enabling Micro-Second Simulations", APS March Meeting, March 2020.
- M.A. Cusentino, M.A. Wood, and A.P. Thompson, "Molecular Dynamics Modeling of Mixed Materials in Tungsten", TMS, San Diego, CA, February 23-27, 2020.
- G. Diamond, C.W. Smith, C. Zhang, E.S. Yoon, G. Gopakumar, O. Sahni, M.S. Shephard, "Unstructured Mesh PIC Framework for GPUs", SIAM Parallel Processing Conf., Seattle, WA, Feb. 15, 2020.
- C.W. Smith, G. Diamond, C. Zhang, E.S. Yoon, G. Perumpilly, M.O. Bloomfield, O. Sahni, and M.S. Shephard, "Progress on the Development of Unstructured Mesh PIC for Fusion Applications", SIAM Parallel Processing Conf., Seattle, WA, Feb. 13, 2020.
- K. Distefano, B. S. Laufer, and K. D. Hammond, "Effects of neutron-induced displacement cascades on helium bubbles in tungsten" 2020 Emerging Researchers National (ERN) Conference in STEM, Washington, DC, February 6–8, 2020.

2019 (May – December):

- Gerrett Diamond, Cameron W. Smith, Chonglin Zhang, Eisung Yoon, Gopan Perumpilly, Onkar Sahni, and Mark S. Shephard "Towards Accelerated Unstructured Mesh Particle-in-Cell", In proceedings of the 10th Workshop on Latest Advances in Scalable Algorithms for Large-Scale Systems (ScalA'19) at the The International Conference for High Performance Computing, Networking, Storage and Analysis (SC19), Denver, Colorado, November 18, 2019.
- A. Weerasinghe, L. Hu, D. Dasgupta, K. D. Hammond, B. D. Wirth, and D. Maroudas. "Defect Interaction Energetics and Stress State of Plasma-Exposed Tungsten." American Institute of Chemical Engineers (AICheE) Annual Meeting, Orlando, Florida, November 13, 2019.
- K. D. Hammond, Z. Yang, D. Maroudas, and B. D. Wirth. "Helium Aggregation and Surface Morphology Near Surfaces and Grain Boundaries in Plasma-Facing Tungsten." American Institute of Chemical Engineers (AIChE) Annual Meeting, Orlando, Florida, November 13, 2019.

- K. D. Hammond, D. Maroudas, and B. D. Wirth. “Model of Helium Bubble Density and Growth in Tungsten from Equations of State.” American Institute of Chemical Engineers (AIChE) Annual Meeting, Orlando, Florida, November 13, 2019.
- D. Martin, K. D. Hammond, and B. D. Wirth. “Large Scale MD Study of the Effect of a Helium Bubble Layer on Hydrogen Diffusion in Tungsten.” International Conference on Fusion Reactor Materials (ICFRM), San Diego, California, October 31, 2019.
- G. Diamond, C.A. Smith and M.S. Shephard, “Particle-grid interaction for exascale PIC”, Joint US-Japan Workshop on PostK-ECP Collaboration and JIFT Exascale Computing Collaboration, Kobe, Japan, October 29, 2019.
- M.A. Cusentino, M.A. Wood, and A.P. Thompson, "Molecular Dynamics Modeling of Mixed Materials in Tungsten Using Machine Learned Interatomic Potentials", ICFRM, La Jolla, CA, October 27 - November 1, 2019.
- T. Casey, K. Sargsyan and H. Najm, “Uncertainty Quantification Workflows in Fusion Plasma Surface Interaction Modeling”, 61st Annual Meeting of the APS Division of Plasma Physics, Fort Lauderdale, Florida, October 21-25, 2019
- C. Zhang, G. Perumpilly, G. Diamond, C. Smith, O. Sahni, A. Truszkowska, and M. Shephard, "An Unstructured Mesh Based Infrastructure for Exascale PIC Simulations", 61st Annual Meeting of the APS Division of Plasma Physics, Fort Lauderdale, Florida, October 21-25, 2019
- M.-F. Huq, V. Vittal-Srinivasaragavan, O. Sahni, and D. Curreli, “Nonuniform Mesh Based hPIC Code for Efficient Scrape-Off-Layer Computation”, Bull. Am. Phys. Soc. 61th Annual Meeting of the APS Division of Plasma Physics, NP10.21, Fort Lauderdale, Florida, October 21-25, 2019
- M. Mustafa, D. Curreli, P. Seleson, C. Hauck, and D. Bernholdt, “Verification and UQ activities of the Particle-In-Cell code hPIC for Near Surface Plasma Conditions”, Bull. Am. Phys. Soc. 61th Annual Meeting of the APS Division of Plasma Physics, CO7.6, Fort Lauderdale, Florida, October 21-25, 2019
- R. D. Smirnov, S. I. Krasheninnikov, M. V. Umansky, I. Joseph, T. D. Rognlien, and J. Guterl, “Coupled modeling of wall retention and plasma edge dynamics”, 7th International Workshop on Plasma Material Interaction Facilities for Fusion Research, La Jolla, CA, October 22-25, 2019
- J. Guterl, T. Abrams, D. Ennis, C. Johnson S. Loch, D.Rudakov, W. Wampler, and P. Snyder, “Analysis and model validation of tungsten prompt redeposition in tokamak divertor”, 61st Annual Meeting of the APS Division of Plasma Physics, Fort Lauderdale, Florida, October 21–25, 2019
- J. Drobny and D. Curreli, “Particle-particle simulations of plasma-material interactions”, Bull. Am. Phys. Soc. 61th Annual Meeting of the APS Division of Plasma Physics, PO6.11, Fort Lauderdale, Florida, October 21-25, 2019
- Davide Curreli, “Multi-Physics Modeling of Plasma- Surface Interactions in ITER (invited), International School on Cold Plasmas: Fundamentals and Applications”, Ettore Majorana Foundation and Centre for Scientific Culture, Erice, Sicily, Sept 12, 2019
- R. D. Smirnov, S. I. Krasheninnikov, M. V. Umansky, I. Joseph, T. D. Rognlien, and J. Guterl, “Time-dependent modeling of coupled plasma-wall dynamics during transient heat load events”, 17th International Workshop on Plasma Edge Theory in Fusion Devices, La Jolla, CA, August 19-21, 2019
- K. Sargsyan, T. Younkin, T. Casey, H. N. Najm, and B. D. Wirth, "Uncertainty Quantification and Propagation for Impurity Migration", Poster presentation at SciDAC PI Meeting, Rockville, MD, July 16-18, 2019.
- A. Lasa, S. Blondel, G. Shaw, T. Younkin, B.D. Wirth, D. Bernholdt, J.M. Canik, M.R. Cianciosa, W. Elwasif, D.L. Green, P.C. Roth, D. Curreli, J. Drobny, M. Baldwin, R.P. Doerner, and D. Nishijima, “Integrated, multi- physics modeling of erosion, redeposition and gas retention in the ITER divertor”, 17th International Conference on Plasma-Facing Materials and Components for Fusion Applications, Eindhoven, the Netherlands, May 21-24, 2019
- J. Guterl, S. Bringuier, R.D. Smirnov, and P. Snyder, “Characterization of wall response to plasma fluctuations in tokamak”, 17th International Conference on Plasma-Facing Materials and Components for Fusion Applications, Eindhoven, the Netherlands, May 21-24, 2019

- A. Weerasinghe, L. Hu, B. D. Wirth, and D. Maroudas, "Effects of Helium Ion Irradiation on Thermal Properties of Tungsten," 17th International Conference on Plasma Facing Materials and Components for Fusion Applications, May 2019, Eindhoven, the Netherlands.
- A. Weerasinghe, L. Hu, K. D. Hammond, B. D. Wirth, and D. Maroudas, "Analysis of Helium Segregation on Surfaces of Tungsten at Different Levels of Helium Ion Irradiation," 17th International Conference on Plasma Facing Materials and Components for Fusion Applications, May 2019, Eindhoven, the Netherlands.
- D. Dasgupta, R. D. Kolasinski, C.-S. Wong, D. Maroudas, and B. D. Wirth, "Modeling of 'Fuzz' Formation in Plasma-Facing Materials," 17th International Conference on Plasma Facing Materials and Components for Fusion Applications, May 2019, Eindhoven, the Netherlands.
- R. D. Kolasinski, D. Dasgupta, C.-S. Wong, R. W. Friddle, A. Engel, J. A. Whaley, D. A. Buchenauer, D. Maroudas, and B. D. Wirth, "Effects of Low-Fluence Helium Plasma Exposure Characterized by Helium Ion Microscopy, Scaning Probes, and Ellipsometry," 17th International Conference on Plasma Facing Materials and Components for Fusion Applications, May 2019, Eindhoven, the Netherlands.
- S. Blondel, D.E. Bernholdt, J.M. Canik, M.R. Cianciosa, D. Curreli, R.P. Doerner, J. Drobny, W. Elwasif, D.L. Green, A. Lasa, D. Nishijima, P.C. Roth, G. Shaw, T. Younkin, and B.D. Wirth, "Prediction of gas bubble evolution under the surface of the ITER divertor with cluster dynamics," 17th International Conference on Plasma-Facing Materials and Components for Fusion Applications, May 2019, Eindhoven, the Netherlands.
- D. Dasgupta, R. D. Kolasinski, C.-S. Wong, D. Maroudas, and B. D. Wirth, "Modeling of Surface Morphological Evolution of Plasma-Facing Tungsten,"19th International Conference on Fusion Reactor Materials (ICFRM-19), October-November 2019, La Jolla, California.
- D. Dasgupta, R. D. Kolasinski, S. Blondel, D. Maroudas, and B. D. Wirth, "Modeling of Helium Retention and Bubble Bursting in Low-Energy Helium Plasma-Exposed Tungsten," 19th International Conference on Fusion Reactor Materials (ICFRM-19), October-November 2019, La Jolla, California.
- D. Dasgupta, R. D. Kolasinski, D. Maroudas, and B. D. Wirth, "On the Onset of 'Fuzz' Formation in Plasma-Facing Materials. I. Surface Morphological Evolution Model," AIChE Annual Meeting, November 2019, Orlando, Florida.
- D. Dasgupta, R. D. Kolasinski, S. Blondel, A. Weerasinghe, D. Maroudas, and B. D. Wirth, "On the Onset of 'Fuzz' Formation in Plasma-Facing Materials. II. Effects of Subsurface Bubble Dynamics, Temperature, and Elastic Moduli of Damaged Tungsten," American Institute of Chemical Engineers (AIChE) Annual Meeting, November 2019, Orlando, Florida.
- A. Weerasinghe, B. D. Wirth, and D. Maroudas, "Thermomechanical Properties of Plasma-Exposed Tungsten," American Institute of Chemical Engineers (AIChE)Annual Meeting, November 2019, Orlando, Florida.